Doctoral Dissertation

In-situ TEM observation of electron irradiation gate effect in MoS_2 nanoribbon channels

CHEN, Limi

Supervisor: Yoshifumi OSHIMA

Graduate School of Advanced Science and Technology

Japan Advanced Institute of Science and Technology

[Materials Science]

September 2025

Abstract

In-situ TEM observation of electron irradiation gate effect in MoS_2 nanoribbon channels

Limi Chen (Oshima Laboratory)
s2220432

In-situ transmission electron microscopy (TEM) provides a powerful platform for probing the electrical behavior of two-dimensional (2D) devices under simultaneous structural observation. However, conventional gating methods are incompatible with electron-transparent TEM holders. Here, we demonstrate a non-contact gating strategy by focusing a scanning transmission electron microscope (STEM) beam onto the SiN_x substrate adjacent to a few-layer MoS_2 channel.

We successfully fabricated a MoS_2 nanoribbon device on a 50 nm SiN_x film designed for TEM observation. During characterization, we observed that the drain-source current I_{ds} increased upon irradiation by a sharp electron probe positioned 15 μm away from the MoS_2 nanoribbon. This increase in I_{ds} was found to correlate positively with the electron beam current I_{beam}, eventually reaching a saturation value.

This behavior mirrors the I_{beam} dependence of positive charge accumulation in the SiN_x film, attributed to the emission of secondary electrons induced by electron beam irradiation. The results indicate that the accumulated positive charges in the SiN_x film electrostatically induce negative carriers in the MoS_2 channel, thereby modulating its conductance. Notably, we observed an immediate increase in I_{ds} concurrent with the initiation of electron beam irradiation and a gradual exponential decay in I_{ds} with a time constant $\tau \approx 90$ s after turning the beam off. Such a long time constant could be confirmed by impedance spectroscopy measurements.

These findings provide compelling evidence that the SiN_x film becomes positively charged due to electron beam irradiation. This charging effect acts analogously to a gate in a field-effect transistor, enabling remote and damage-free modulation of the MoS_2 channel. Thus, sharp electron beam irradiation of the SiN_x film can function effectively as an indirect gate. This approach presents a valuable technique for evaluating the electrical properties of 2D materials without subjecting them to direct irradiation damage.

Keywords: *in-situ* TEM, indirect electron beam gating, MoS_2 based-device, dielectric charging, Schottky contact

Contents

Chapter 1 Background

Introduction

This chapter introduces the primary focus of the thesis: the study of two terminal MoS_2 device using *in-situ* transmission electron microscopy (TEM) with electron beam gating. It outlines how advanced *in-situ* TEM techniques can be utilized to explore electrical modulation mechanisms in nanoscale devices.

In Chapter 1.1, we introduce the material properties of MoS_2 that make it a promising candidate for next-generation electronic applications. In Chapter 1.2, we review conventional strategies for modulating the electrical properties of MoS_2-based devices, and identify their key limitations. In Chapter 1.3, we introduce *in-situ* TEM as a multifunctional experimental platform for studying MoS_2 -based devices. We discusses the evolution of *in-situ* TEM techniques, and highlights their unique ability to reveal correlations between atomic structure and device performance. In Chapter 1.4, we outline a new approach of indirect electron beam gating and define the purpose of this thesis.

1.1 Transition metal dichalcogenides (TMDCs) and MoS_2

The discovery of graphene in 2004[1] opened up the initial surge of interest in two-dimensional (2D) layered materials. These magical layered materials consist of atomically thin sheets stacked by weak van der Waals interactions, in contrast to the strong covalent or ionic bonds that hold atoms together within each layer. This bonding allows bulk crystals to be straightforwardly exfoliated into monolayers, enabling access to novel low-dimensional material systems. It helps pave the way to the emergence of qualitatively new effects not present in the three-dimensional world.

Under ideal conditions, graphene exhibits the highest carrier mobility among all 2D layered materials, with reported values exceeding 10^5 $cm^2/V \cdot s$.[2] Despite its outstanding transport properties, the absence of an intrinsic bandgap severely restricts graphene's utility in digital logic applications where high on/off current ratios are essential. This limitation prompted the search for alternative 2D semiconductors that inherently possess a finite bandgap suitable for electronic switching.

Among the candidates explored, transition metal dichalcogenides (TMDCs) have attracted considerable attention. TMDCs are layered materials with a general formula of MX_2, where M represents a transition metal (e.g., Mo, W) and X denotes a chalcogen atom (e.g., S, Se, Te). Historically, TMDCs were studied mainly for their tribological

properties as solid lubricants.[3] Renewed interest arose when their semiconducting properties, particularly in monolayer forms, were recognized to be highly suitable for nanoscale electronic applications.[4]

Molybdenum disulfide (MoS_2), a prototypical member of the TMDC family, stands out due to its desirable combination of material properties. Bulk MoS_2 possesses an indirect bandgap of approximately 1.2 eV, while monolayer MoS_2 exhibits a direct bandgap of around 1.8 eV,[5,6] making it highly attractive for applications in field-effect transistors (FETs), photodetectors, and spintronic devices.

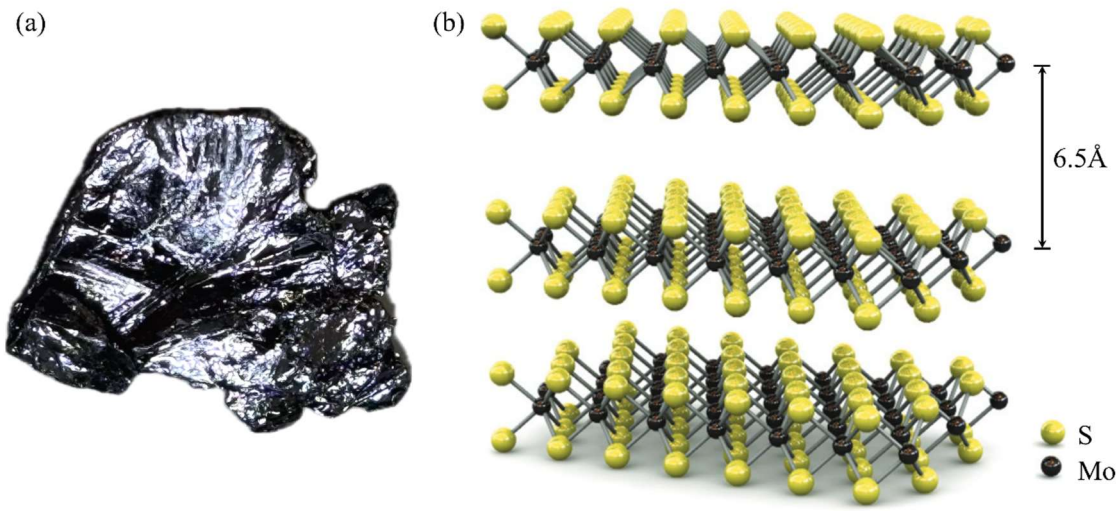

Figure 1.1 (a) Photograph of bulk MoS_2 crystal. (b) Atomic structure of MoS_2 with an interlayer distance of 6.5Å.

MoS_2 was first artificial synthesized in the 1936s,[7] and its layered structure was characterized through various experimental techniques over subsequent decades. The most stable crystal structure is the 2H phase, which exhibits semiconducting behavior, whereas other metastable phases, such as 1T and 1T' are metallic.[8–10] This feature enables tunable optical and electrical behaviors that are highly desirable for device engineering. Furthermore, Theoretical calculations based on first-principles suggest that the phonon-limited mobility in intrinsic n-type single-layer MoS_2 at room temperature is estimated to be approximately 410 $cm^2 \cdot V^{-1} \cdot s^{-1}$, supporting its potential for high-performance electronic and optoelectronic devices.[11]

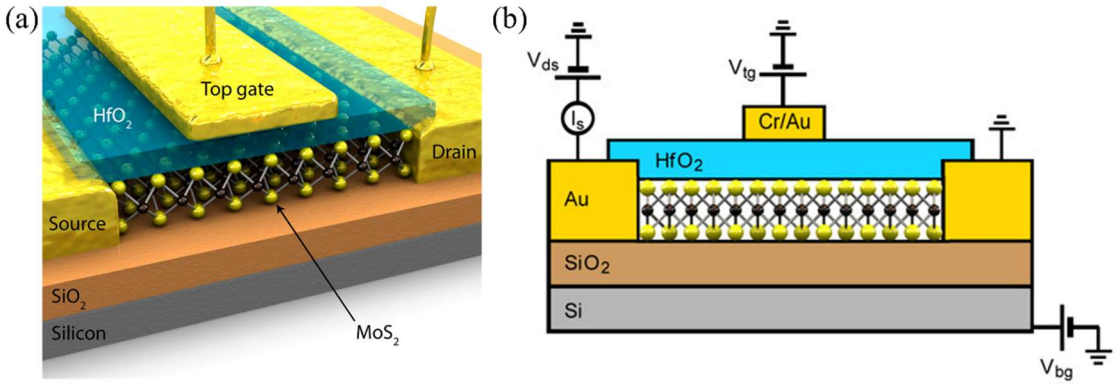

Figure 1.2 (a) Schematic view and (b) cross-sectional view of the single-layer MoS_2 FET.

A major milestone in the development of MoS_2 electronics was reported by Radisavljevic et al. in 2011,[12] who demonstrated a high-performance single-layer MoS_2

field-effect transistor with an on/off current ratio exceeding 10^8 and ultralow power consumption. This pioneering work triggered an explosion of research into MoS_2-based devices, ranging from logic circuits to neuromorphic computing elements,[13] as shown in Figure1.3.[13]

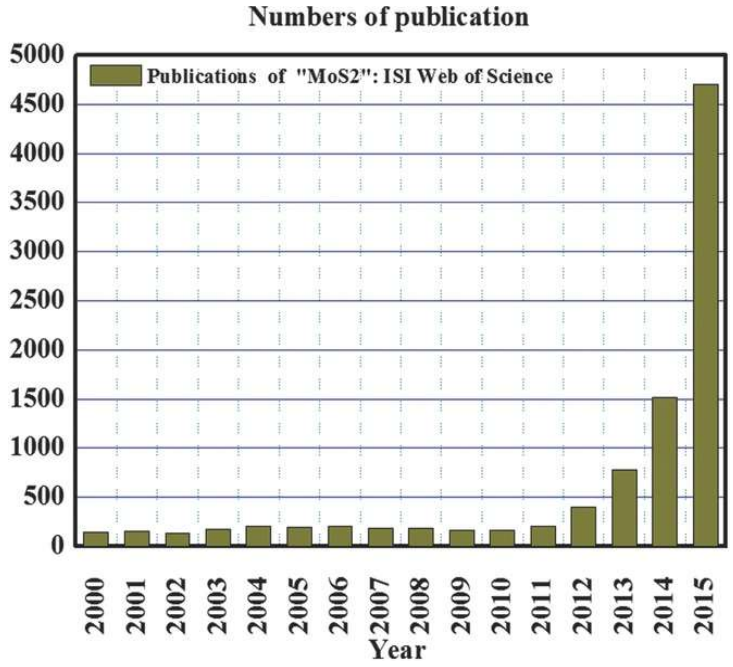

Figure 1.3 Publications on MoS_2 from 2000 to 2015. [13]

Despite recent advances, it remains challenging to achieve precise and controllable modulation of MoS_2 electrical properties without inducing detrimental defects or relying on complex fabrication steps.[14] In the next chapter, we review the development of existing techniques such as chemical doping, electrostatic gating, and phase engineering, and critically examine their inherent limitations. These insights motivate the development of *in-situ* and non-invasive strategies discussed in this study.

1.2 Electrical modulation of MoS_2-based devices

To address the challenges highlighted above, researchers have explored a wide spectrum of strategies for tuning the electrical properties of MoS_2. Chemical doping and phase engineering[15] have been extensively studied for modulating MoS_2 electrical properties. But both suffer from inherent challenges. Doping may create structural defects that scatter charge carriers, substantially reducing mobility through mechanisms including charged impurity scattering.[16] Besides, these defects elevate contact resistance and contribute to spatial inhomogeneity in electronic properties.[17] Phase engineering between 2H and 1T states requires strains exceeding the elastic limit of MoS_2, resulting in irreversible structural transformations.[18] These limitations produce devices with poor uniformity, stability, and reliability, hindering practical applications.

Gate control remains the most effective method for tuning carrier density in MoS_2-based devices. Solid-state gates use dielectric materials such as SiO_2, Al_2O_3, or HfO_2 to achieve moderate carrier density modulation through field effects. For instance, sub-10 nm Al_2O_3 layers deposited via remote oxygen plasma pretreatment on MoS_2have yielded devices with gate leakage currents as low as 0.1 pA/μm^2 under fields up to 4.5 MV/cm.[19] Dual-gate architectures offer enhanced electrostatic tunability in MoS_2 devices by enabling independent control of carrier density and threshold voltage. Yet mobility

extraction in such structures can be affected by inter-gate capacitive coupling, potentially leading to overestimated values.[20] Ionic liquid gating enables higher carrier densities by forming electric double layers (EDLs) on both surfaces of suspended MoS_2 devices, achieving a coupling efficiency of approximately 4.6×10^{13} $cm^{-2} \cdot V^{-1}$.[21] However, conventional gate approaches often involve complex fabrication procedures, risk inducing electrochemical side reactions, and may still fall short of delivering the high carrier densities required for certain applications. In summary, despite the growing variety of modulation strategies, achieving defect-free, reversible, and scalable control over MoS_2 electrical behavior remains challenging.

In addition, a fundamental limitation of current methods is the inability to directly observe the dynamic processes occurring during carrier density modulation in real time. Most existing characterization methods rely on "before and after" measurements that fail to capture the evolution of charge distribution, interface response, and transient phenomena during the modulation process itself. This limitation in spatial and temporal resolution is particularly pronounced at the nanoscale, especially when studying key phenomena such as interface modulation dynamics, Schottky barrier evolution, and charge trapping behavior.

In response to these challenges, *in-situ* transmission electron microscopy (TEM) has

emerged as a powerful platform that enables atomic-scale imaging in conjunction with electrical measurements. Recent studies have demonstrated that a sharply focused TEM electron beam can serve as a local gate, enabling dynamic, reversible control of MoS_2 channel conductance without direct beam exposure or structural damage.[22] The next section introduces this emerging *in-situ* beam gating strategy in detail, highlighting its unique advantages and potential as a novel approach for modulating 2D semiconductor devices.

1.3 *In-situ* TEM: a multifunctional platform for 2D devices

1.3.1 Brief introduction of TEM

Since its invention in the 1930s,[23] TEM has become an indispensable technique in materials science due to its exceptional spatial resolution and ability to reveal atomic-scale structures. The fundamental advantage of TEM over conventional optical microscopy lies in the wave nature of electrons. As first proposed by De Broglie[24] in 1925 and later confirmed experimentally,[25,23] electrons exhibit wave-like behavior, with a wavelength inversely proportional to the square root of their energy. This means that an accelerated electron can have a wavelength several orders of magnitude shorter than that of visible light, which directly translates to a much higher theoretical resolving power.

According to the Rayleigh criterion, the smallest resolvable distance δ is proportional to the radiation wavelength λ as the following equation 1-1:

$$\delta = \frac{0.61\lambda}{\mu sin\beta} \quad 1\text{-}1$$

where $\mu sin\beta$ corresponds to the numerical aperture of the lens. While visible light (390–700 nm) limits the resolution of optical microscopes to around 200 nm, a 300 keV electron has a wavelength of approximately 3pm.[26] In practice, however, resolution is constrained by lens aberrations, electron source coherence, and mechanical stability. Modern aberration-corrected TEMs equipped with cold field-emission sources routinely achieve spatial resolutions below 0.1 nm. This capability is particularly crucial in the study of 2D materials including MoS_2, where atomic arrangements, grain boundaries, and layer thickness can drastically influence device performance.

TEM instruments typically operate in two primary modes: conventional TEM mode and scanning transmission electron microscopy (STEM) mode, as is shown in Figure1.4. While conventional TEM uses a parallel electron beam to illuminate the sample and form contrast-rich images via transmitted intensity, STEM employs a tightly focused electron probe that raster-scans the specimen point-by-point. This scanning approach allows not only for high-resolution imaging but also for simultaneous acquisition of analytical signals, such as energy-dispersive X-ray spectroscopy (EDS) and electron energy-loss

spectroscopy (EELS), making STEM a highly versatile technique.

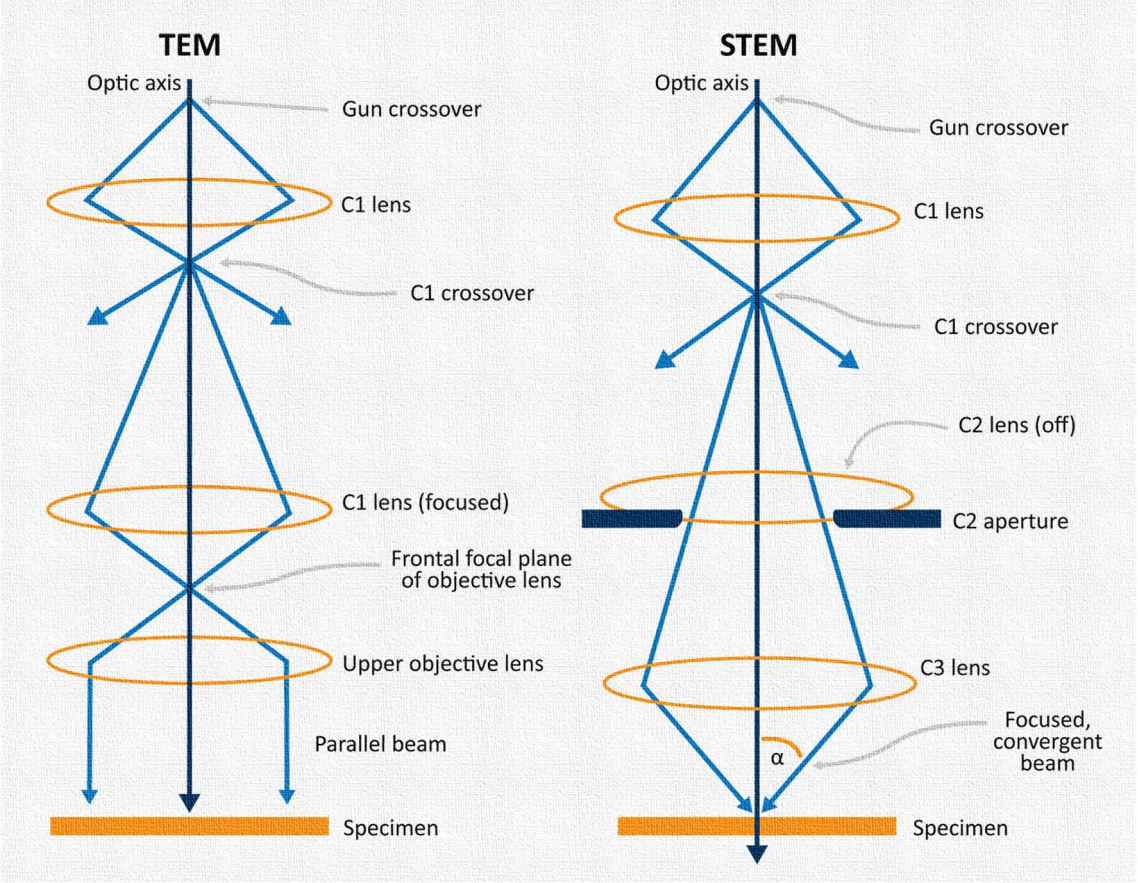

Figure 1.4 Configuration of the microscope in TEM mode (left) and STEM mode (right).[27]

One particularly useful operation within STEM is the "spot mode," in which the electron beam is held stationary at a selected position rather than scanned across the sample. By tuning the condenser lens system, the convergence angle of the electron beam is precisely adjusted to achieve a sub-nanometer probe with high current density. This spot-mode functionality enables localized electron irradiation, offering fine spatial control for perturbing materials and probing their dynamic responses in a controlled, site-

specific manner. The STEM spot mode plays a central role in our study, where it is used not to directly irradiate the MoS_2 device but to target nearby regions of the underlying SiN_x membrane. This configuration avoids direct beam-induced damage while enabling modulation of the MoS_2 channel conductance through substrate charging effects.

1.3.2 In-situ TEM

In-situ TEM provide an indispensable platform for 2D electronic systems, because of its capability to combine atomic resolution imaging with simultaneous electrical, mechanical and thermal measurements.[28-30] This capability addresses a critical gap in conventional device measurements, which relies on only static "before-and-after" comparison and obscure the transient dynamics of charge transport, interface evolution, or defect generation.[28] Benefit from its spatially selective, and temporally resolved ability, *in-situ* TEM can help mechanistic understanding of how atomic-scale processes govern material properties in 2D devices. For instance, *in-situ* TEM electrical measurements of graphene nanoribbon devices using specialized electrical biasing holders enable simultaneous characterization of electrical performance and atomic structure.[31,32]

Despite its advantages, most *in-situ* TEM electrical measurements have been limited to two-terminal configurations, as conventional gating methods such as top or back gates are generally incompatible with the electron-transparent design of TEM chips. These

gating structures either obstruct the electron beam path or introduce parasitic background signals. While side-gate designs have been proposed, their fabrication on TEM chips remains non-trivial and often requires customization.[33]

Recent advances have turned to the TEM electron beam itself as a potential gate modulation tool. Direct irradiation, where the electron beam is focused directly onto the 2D material, has been reported to modulate device conductance.[34,35] However, high-energy electron irradiation (80keV-300keV) can produce irreversible structural changes to 2D materials, including vacancy, dislocation and interlayer displacement.[36] Furthermore, prolonged beam exposure can lead to the accumulation of amorphous hydrocarbon layers on the 2D surface, which may interfere with electrical measurements.[37]

Indirect electron beam gating was recently proposed as a promising alternative. In two-terminal MoS_2 device, the TEM beam is focused not on the MoS_2 channel but on its adjacent dielectric SiN_x substrate.[38] Remarkably, such indirect beam irradiation led to a pronounced, reversible modulation of the channel conductance. These findings suggest that interaction between the electron beam and the substrate can act as a virtual gate. However, existing indirect beam gating schemes rely on conventional TEM irradiation, which exposes a broad area and may include the 2D channel. This can trigger undesired

responses in photoresponsive materials such as MoS_2. In addition, the mechanism of indirect beam gating is not yet fully understood and requires further investigation.

1.4 Purpose

In this study, we explored a novel electron beam gating strategy in which a focused STEM beam was directed onto the SiN_x substrate near a suspended MoS_2 channel. Without directly contacting the device, the electron beam induced localized charging in the supporting SiN_x layer, effectively modulating the carrier density and conductance of the MoS_2. We systematically investigated this effect by varying beam current strength and analyzed its mechanism. This setup allowed us to decouple beam-induced substrate effects from direct beam damage, offering a non-invasive, spatially resolved, and temporally continuous method to study charge modulation mechanisms in 2D devices.

Reference

[1] Novoselov, K. S.; Geim, A. K.; Morozov, S. V.; Jiang, D.; Zhang, Y.; Dubonos, S. V.; Grigorieva, I. V.; Firsov, A. A. Electric Field Effect in Atomically Thin Carbon Films. *Science* **2004**, *306* (5696), 666–669. https://doi.org/10.1126/science.1102896.

[2] Geim, A. K.; Novoselov, K. S. The Rise of Graphene. *Nat. Mater.* **2007**, *6* (3), 183–191. https://doi.org/10.1038/nmat1849.

[3] Vazirisereshk, M. R.; Martini, A.; Strubbe, D. A.; Baykara, M. Z. Solid Lubrication with MoS_2: A Review. *Lubricants* **2019**, *7* (7), 57. https://doi.org/10.3390/lubricants7070057.

[4] Wang, Q. H.; Kalantar-Zadeh, K.; Kis, A.; Coleman, J. N.; Strano, M. S. Electronics and Optoelectronics of Two-Dimensional Transition Metal Dichalcogenides. *Nat. Nanotechnol.* **2012**, *7* (11), 699–712. https://doi.org/10.1038/nnano.2012.193.

[5] Mak, K. F.; Lee, C.; Hone, J.; Shan, J.; Heinz, T. F. Atomically Thin MoS_2: A New Direct-Gap Semiconductor. *Phys. Rev. Lett.* **2010**, *105* (13), 136805. https://doi.org/10.1103/PhysRevLett.105.136805.

[6] Splendiani, A.; Sun, L.; Zhang, Y.; Li, T.; Kim, J.; Chim, C.-Y.; Galli, G.; Wang, F. Emerging Photoluminescence in Monolayer MoS_2. *Nano Lett.* **2010**, *10* (4), 1271–1275. https://doi.org/10.1021/nl903868w.

[7] Yagoda, H.; Fales, H. A. The Separation and Determination of Tungsten and Molybdenum. *J. Am. Chem. Soc.* **1936**, *58* (8), 1494–1501. https://doi.org/10.1021/ja01299a051.

[8] Mattheiss, L. F. Band Structures of Transition-Metal-Dichalcogenide Layer Compounds. *Phys. Rev. B* **1973**, *8* (8), 3719–3740. https://doi.org/10.1103/PhysRevB.8.3719.

[9] Wypych, F.; Schöllhorn, R. 1T- MoS_2, a New Metallic Modification of Molybdenum Disulfide. *J. Chem. Soc. Chem. Commun.* **1992**, No. 19, 1386–1388. https://doi.org/10.1039/C39920001386.

[10] Liu, L.; Wu, J.; Wu, L.; Ye, M.; Liu, X.; Wang, Q.; Hou, S.; Lu, P.; Sun, L.; Zheng, J.; Xing, L.; Gu, L.; Jiang, X.; Xie, L.; Jiao, L. Phase-Selective Synthesis of 1T′ MoS_2 Monolayers and Heterophase Bilayers. *Nat. Mater.* **2018**, *17* (12), 1108–1114. https://doi.org/10.1038/s41563-018-0187-1.

[11] Kaasbjerg, K.; Thygesen, K. S.; Jacobsen, K. W. Phonon-Limited Mobility in n-Type Single-Layer MoS${}_{2}$ from First Principles. *Phys. Rev. B* **2012**, *85* (11), 115317. https://doi.org/10.1103/PhysRevB.85.115317.

[12] Radisavljevic, B.; Radenovic, A.; Brivio, J.; Giacometti, V.; Kis, A. Single-Layer MoS_2 Transistors. *Nat. Nanotechnol.* **2011**, *6* (3), 147–150.

https://doi.org/10.1038/nnano.2010.279.

[13] Pham, V. P.; Yeom, G. Y. Recent Advances in Doping of Molybdenum Disulfide: Industrial Applications and Future Prospects. *Adv. Mater.* **2016**, *28* (41), 9024–9059. https://doi.org/10.1002/adma.201506402.

[14] Jariwala, D.; Sangwan, V. K.; Lauhon, L. J.; Marks, T. J.; Hersam, M. C. Emerging Device Applications for Semiconducting Two-Dimensional Transition Metal Dichalcogenides. *ACS Nano* **2014**, *8* (2), 1102–1120. https://doi.org/10.1021/nn500064s.

[15] Eda, G.; Fujita, T.; Yamaguchi, H.; Voiry, D.; Chen, M.; Chhowalla, M. Coherent Atomic and Electronic Heterostructures of Single-Layer MoS_2. *ACS Nano* **2012**, *6* (8), 7311–7317. https://doi.org/10.1021/nn302422x.

[16] Wani, S.-S.; Hsu, C. C.; Kuo, Y.-Z.; Darshana Kumara Kimbulapitiya, K. M. M.; Chung, C.-C.; Cyu, R.-H.; Chen, C.-T.; Liu, M.-J.; Chaudhary, M.; Chiu, P.-W.; Zhong, Y.-L.; Chueh, Y.-L. Enhanced Electrical Transport Properties of Molybdenum Disulfide Field-Effect Transistors by Using Alkali Metal Fluorides as Dielectric Capping Layers. *ACS Nano* **2024**, *18* (16), 10776–10787. https://doi.org/10.1021/acsnano.3c11025.

[17] McDonnell, S.; Addou, R.; Buie, C.; Wallace, R. M.; Hinkle, C. L. Defect-

Dominated Doping and Contact Resistance in MoS_2. *ACS Nano* **2014**, *8* (3), 2880–2888. https://doi.org/10.1021/nn500044q.

[18] Cheng, P.; Sun, K.; Hu, Y. H. Mechanically-Induced Reverse Phase Transformation of MoS_2 from Stable 2H to Metastable 1T and Its Memristive Behavior. *RSC Adv.* **2016**, *6* (70), 65691–65697. https://doi.org/10.1039/C6RA12735E.

[19] Yang, W.; Sun, Q.-Q.; Geng, Y.; Chen, L.; Zhou, P.; Ding, S.-J.; Zhang, D. W. The Integration of Sub-10 Nm Gate Oxide on MoS_2 with Ultra Low Leakage and Enhanced Mobility. *Sci. Rep.* **2015**, *5* (1), 11921. https://doi.org/10.1038/srep11921.

[20] Fuhrer, M. S.; Hone, J. Measurement of Mobility in Dual-Gated MoS_2 Transistors. *Nat. Nanotechnol.* **2013**, *8* (3), 146–147. https://doi.org/10.1038/nnano.2013.30.

[21] Wang, F.; Stepanov, P.; Gray, M.; Lau, C. N.; Itkis, M. E.; Haddon, R. C. Ionic Liquid Gating of Suspended MoS_2 Field Effect Transistor Devices. *Nano Lett.* **2015**, *15* (8), 5284–5288. https://doi.org/10.1021/acs.nanolett.5b01610.

[22] Masih Das, P.; Drndić, M. In Situ 2D MoS_2 Field-Effect Transistors with an Electron Beam Gate. *ACS Nano* **2020**, *14* (6), 7389–7397. https://doi.org/10.1021/acsnano.0c02908.

[23] Knoll, M.; Ruska, E. Das Elektronenmikroskop. *Z. Für Phys.* **1932**, *78* (5), 318–339. https://doi.org/10.1007/BF01342199.

[24] Broglie, L. D. Recherches sur la théorie des Quanta. *Ann. Phys.* **1925**, *10* (3), 22–128. https://doi.org/10.1051/anphys/192510030022.

[25] Davisson, C.; Germer, L. H. Diffraction of Electrons by a Crystal of Nickel. *Phys. Rev.* **1927**, *30* (6), 705–740. https://doi.org/10.1103/PhysRev.30.705.

[26] Williams, D. B.; Carter, C. B. The Transmission Electron Microscope. In *Transmission Electron Microscopy: A Textbook for Materials Science*; Williams, D. B., Carter, C. B., Eds.; Springer US: Boston, MA, **1996**; pp 3–17. https://doi.org/10.1007/978-1-4757-2519-3_1.

[27] *Scanning Transmission Electron Microscopy | Nanoscience Instruments*. https://www.nanoscience.com/techniques/scanning-transmission-electron-microscopy/ (accessed 2025-05-21).

[28] C. Chen, T. Zhang, Y. Lei, J. Fan, L. Zhang, G. Wang, L. Gao, P. Li, Q. Zhu, X. Ma and Y. Hao, Appl. Phys. Rev. 2025, 12 (1), 011326. https://doi.org/10.1063/5.0135772.

[29] C. Hou, K. Wang, W. Zhang, D. Chen, X. Wang, L. Fan, C. Li, J. Zhao and L. Dong, Adv. Mater. 2023, 35 (28), 2301439. https://doi.org/10.1002/adma.202301439.

[30] R. Ramachandramoorthy, R. Bernal and H. D. Espinosa, ACS Nano 2015, 9 (5), 4675–4685. https://doi.org/10.1021/acsnano.5b01391.

[31] C. Liu, J. Zhang, M. Muruganathan, H. Mizuta, Y. Oshima and X. Zhang, Carbon

2020, 165, 476–482. https://doi.org/10.1016/j.carbon.2020.04.094.

[32] C. Liu, J. Zhang, X. Zhang, M. Muruganathan, H. Mizuta and Y. Oshima, Nanotechnology 2020, 32 (2), 025710. https://doi.org/10.1088/1361-6528/abaf5f.

[33] J. A. Rodríguez-Manzo, Z. J. Qi, A. Crook, J.-H. Ahn, A. T. C. Johnson and M. Drndić, ACS Nano 2016, 10 (4), 4004–4010. https://doi.org/10.1021/acsnano.6b00920.

[34] Y. Fan, A. W. Robertson, X. Zhang, M. Tweedie, Y. Zhou, M. H. Rummeli, H. Zheng and J. H. Warner, ACS Appl. Mater. Interfaces 2016, 8 (48), 32963–32969. https://doi.org/10.1021/acsami.6b11480.

[35] W. M. Parkin, A. Balan, L. Liang, P. M. Das, M. Lamparski, C. H. Naylor, J. A. Rodríguez-Manzo, A. T. C. Johnson, V. Meunier and M. Drndić, ACS Nano 2016, 10 (4), 4134–4142. https://doi.org/10.1021/acsnano.6b01419

[36] R. F. Egerton, P. Li and M. Malac, Micron 2004, 35 (6), 399–409. https://doi.org/10.1016/j.micron.2004.02.003.

[37] O. Dyck, S. Kim, S. V. Kalinin and S. Jesse, J. Vac. Sci. Technol. B 2018, 36 (1), 011801. https://doi.org/10.1116/1.5008523.

[38] P. M. Das and M. Drndić, ACS Nano 2020, 14 (6), 7389–7397. https://doi.org/10.1021/acsnano.0c02908.

Chapter 2 Preparation of MoS_2 Flakes and Electrode Fabrication

Introduction

This chapter presents the process of preparing high quality MoS_2 flakes and depositing electrodes for *in-situ* electrical measurements. In Chapter 2.1, we describe the exfoliation of MoS_2 flakes and their optical identification on SiO_2/Si substrates. In Chapter 2.2, we introduce the design and structure of the customized TEM chip used for electrical measurements. In Chapter 2.3, we explain the electrode fabrication process, including substrate cleaning, resist coating, electron beam lithography, metal deposition, and lift-off.

2.1 Exfoliation and Optical Identification of MoS_2

According to chapter 1, high-quality MoS_2 flakes suitable for device fabrication and *in-situ* TEM analysis must meet several strict criteria: they must be thin (ideally monolayer or few-layer), clean (with minimal surface residues), compact in lateral size (within 10 μm) and uniformly. Among various material preparation strategies, mechanical exfoliation remains one of the most effective methods for producing 2D flakes with pristine structure and minimal contamination, especially when high-mobility or defect-sensitive devices are desired.

Mechanical exfoliation was originally developed by Andre Geim and Konstantin Novoselov for the isolation of monolayer graphene in 2004.[1] involves peeling layered crystals apart using adhesive tapes, making use of the weak van der Waals forces that bind the layers together. In contrast to chemical vapor deposition (CVD), which often yields large-area but polycrystalline or impurity-laden films, mechanically exfoliated flakes tend to have fewer structural defects, sharper edges, and more uniform electronic properties, making them ideal for fundamental studies and prototyping.

In our study, we began with high-quality bulk MoS_2 crystals purchased from HQ Graphene. A piece of strong adhesive tape (Nitto N-300) was used to exfoliate the crystal, followed by 5–6 successive peelings to fragment and distribute the flakes more finely. .

The tape was then gently brought into contact with a low-residue thermal release tape (Nitto SPV363) to reduce potential contamination. This assembly was finally pressed onto a 285 nm SiO_2-coated Si substrate with the size of 1.5cm × 2cm.

Mechanical exfoliation typically results in a broad distribution of flake sizes and thicknesses on the substrate. Atomically thin flakes are a minority among much thicker crystals, making reliable and efficient identification essential. To achieve this, several techniques can be employed, each with specific advantages and limitations.

Raman spectroscopy is a widely used and non-destructive technique to determine layer number based on the frequency difference between the A_{1g} and E^1_{2g} vibrational modes.[2] However, Raman measurements require focused laser illumination, which may cause localized heating or photochemical effects that degrade the MoS_2 flake, especially in monolayer or lightly doped samples. Atomic force microscopy (AFM) can provide nanometer-precision height measurements, and is often used to calibrate layer number in small regions. Yet, AFM scanning over a centimeter-scale area is highly time-consuming and may be affected by ambient contaminants or polymer residues on the flake, resulting in inaccurate thickness values.

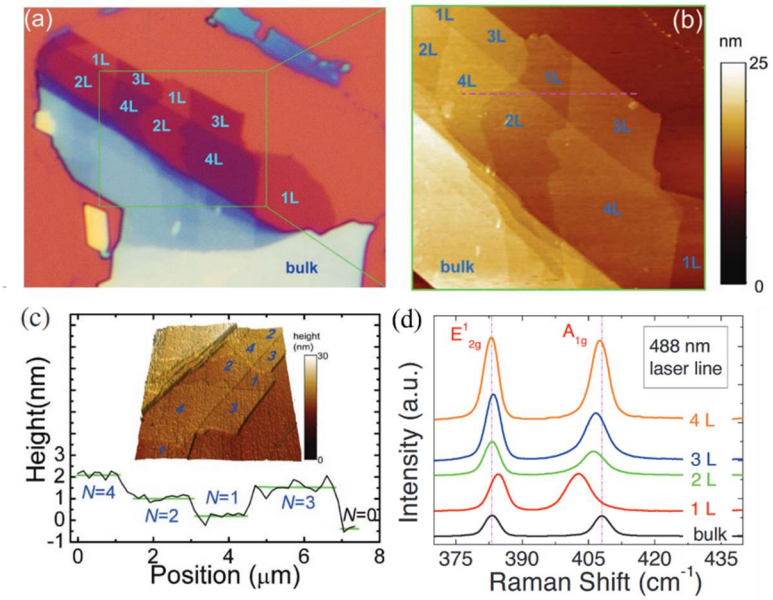

Figure 2.1 (a) Optical image of MoS_2 flake on 285 nm SiO_2-coated Si substrate. (b) AFM height image of the region inside the green square in (a). (c) Height profile along the dashed line in (b). Inset: 3D plot of the AFM height signal. (d) Raman spectra of different locations with various thicknesses on the MoS_2 flake.[2]

Optical microscope selection, in this case, is regarded as the most efficient method which offers the fastest and most practical approach for large-area screening. Due to the light absorption and interference color effects, the MoS_2 flakes with different thickness shows different colors, and their optical contrast can be enhanced while exfoliating flakes on SiO_2/Si substrates with specific thickness, as is shown in the Figure 2.2.[3] The scale bar is 5 μm from 1 layer to 11 layer and 10 μm for the 12 layer flakes. The most common SiO_2 thickness ranges of the Si/SiO_2 substrate are 70-90 nm and 270-300 nm, and the

specific thicknesses are slightly different while identifying different 2D materials.

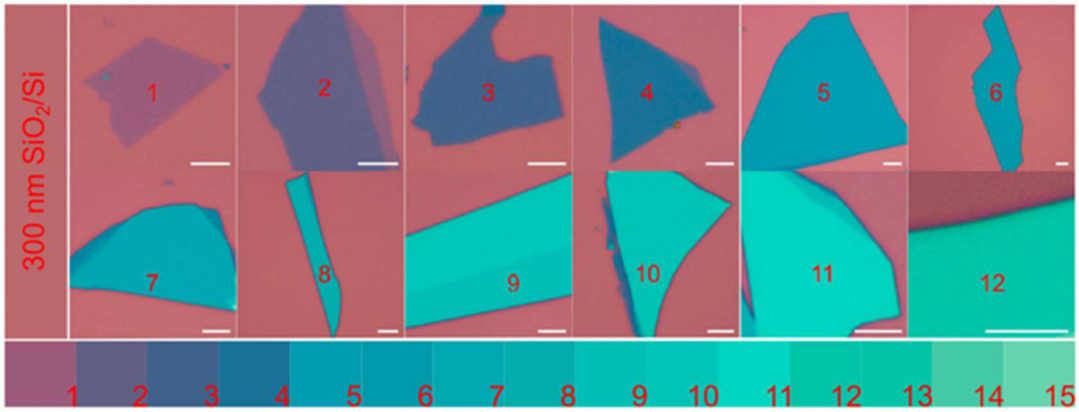

Figure 2.2 Color optical images of 1L−15L MoS_2 on 300 nm SiO_2/Si substrate.[3]

Based on the multi-layer Fresnel reflection method, a multiple-media optical system can be used to explain the optical contrast of flakes, as is shown in Figure 2.3 (a).[4] We suppose the light is illuminated along the normal incidence direction to the sample. The incident light passes crosses the flake and SiO_2 layer until it reaches the Si wafer, and the reflected light passes through the same path and reaches the measuring device detector like a charged-coupled device(CCD) camera. According to the Fresnel law, the reflected light of each interface can be calculated if we know the attenuation and the phase shift introduced by passing through the media.

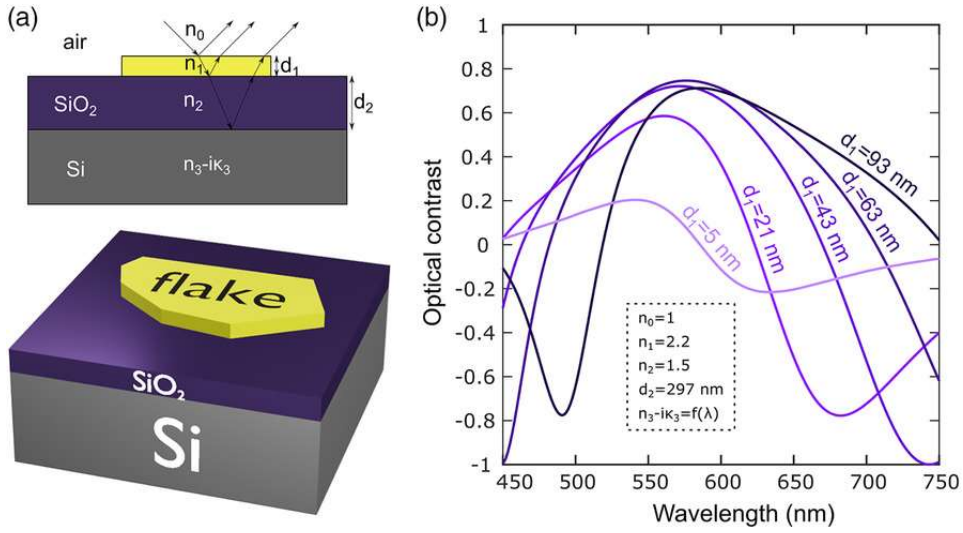

Figure 2.3 (a) A multiple-media optical system for optical contrast Calculation.[4] (b) Optical contrast calculated by the Fresnel law-based model.[5]

The reflected intensity of monochromatic light can be calculated as Equation 2-1.

$$I = \frac{r_{01}e^{i(\phi_1+\phi_2)} + r_{12}e^{-i(\phi_1-\phi_2)} + r_{23}e^{-i(\phi_1+\phi_2)} + r_{01}r_{12}r_{23}e^{i(\phi_1-\phi_2)}}{e^{i(\phi_1+\phi_2)} + r_{01}r_{12}e^{-i(\phi_1-\phi_2)} + r_{01}r_{23}e^{-i(\phi_1+\phi_2)} + r_{12}r_{23}e^{i(\phi_1-\phi_2)}} \qquad 2\text{-}1$$

In this equation, the subindexes 1, 2, and 3 correspond to air, flake, SiO_2, and Si separately. The reflection coefficient is $r_{ij} = \frac{n_i - n_j}{n_i + n_j}$, the phase shift in the medium i is $\phi_i = \frac{2\pi n_i d_i}{\lambda}$, the respective complex refractive is n_i, the thickness is d_i, the wavelength is λ.

Optical contrast (C) defined in Equation (2) can be obtained by referring to the experiment of Frisenda R. et al.[6] By this method, Puebla et al calculated the MoO_3 optical contrast by Fresnel model which fitted well with experimental data.[5]

$$C = \frac{I_f - I_s}{I_f + I_s} \qquad 2\text{-}2$$

Where the reflected intensity on the MoO_3 flake is I_f, the reflected intensity on the bare su6bstrate is I_s. I_f can be calculated according to Equation 1, I_s can be obtained while replacing the medium 1 from flake to air. Figure 1b shows the different optical contrast of flake when the flake thickness changes from 5 to 93nm, and this value is calculated using air as the medium 1. Here, the refractive index for air is$n_0 = 1$; the refractive index for single crystalline MoO_3 flake is $n_1 = 2.2$, ignoring the effect of thickness to MoO_3 band structure; the refractive index for SiO_2 is $n_2 = 1.5$, with the thickness of $d_2 = 297nm$; the refractive index for Si wafer depends on wavelength.

In this research, we use the 285 nm SiO_2-coated Si substrate to identify the layer numbers of MoS_2 flakes. The MoS_2 flakes are exfoliated on SiO_2 substrate, and identified by an optical microscope. Relatively thin layers with the size below 10 μm will be transferred to the electrodes for measurement afterward.

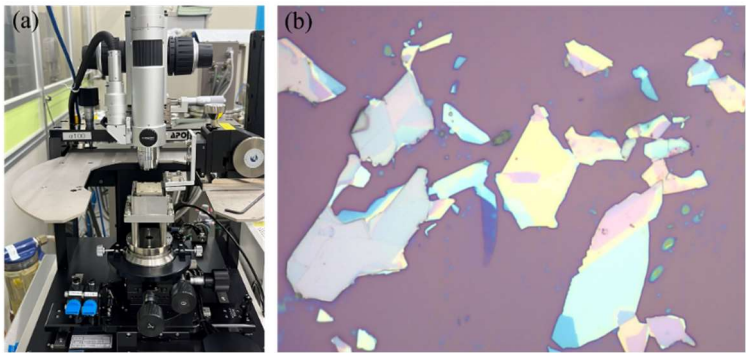

Figure 2.4 (a) Optical microscope for MoS_2 thickness identification. (b) Exfoliated MoS_2 flake on 285 nm SiO_2/Si substrate. The light purple area is the monolayer.

2.2 Electrode fabrication on customed TEM chip

2.2.1 The structure of the customed TEM chip

The customized TEM chip used for electrical measurements was originally developed by C. Liu in our lab.[7–9] It is mounted on the sample stage of a customed *in-situ* TEM holder, as shown in Figure 2.3 (a). The customized TEM chip was fabricated on a 200 μm-thick Si substrate coated with a 50 nm low-stress SiN_x film (Alliance Biosystems). The overall chip size was approximately 2.6 × 2.6 mm. Three 60 × 60 μm square windows were etched to form suspended, electron-transparent SiN_x regions.

Each window is patterned with a pair of source and drain electrodes, 10 μm in width, leaving a 5 μm-wide channel gap at the center. MoS_2 flakes are then transferred across these gaps to create suspended channels for electrical measurements. The SiN_x membranes are insulating, which ensures that current flows only through the MoS_2 flakes bridging the electrodes.

Three MoS_2 samples can be transferred onto the three separate windows on a single chip. Each device can be measured independently, which improves the reliability of the experiment and increases the overall success rate.

This design enables simultaneous fabrication and sequential measurement of multiple devices under identical conditions, helping to verify reproducibility and

minimize sample-to-sample variability. The conductivity change of each MoS_2 channel is measured during indirect electron beam gating by irradiating nearby regions of the SiN_x substrate with different beam strength.

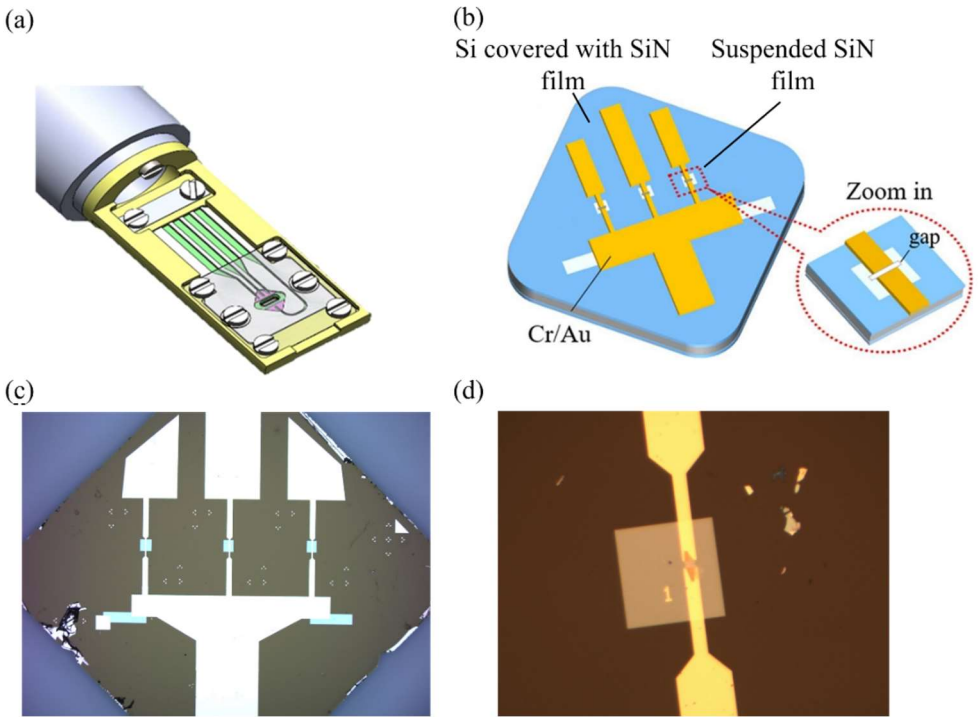

Figure 2.5 (a) Head of the custom TEM holder with electrical connections.[7] (b) Si/SiN_x chip with electrodes.[8] (c) Optical microscope image showing patterned source and drain electrodes. (d) Optical image of a MoS_2 flake bridging the electrode gap.

2.2.2 Electrode fabrication

Electrodes will be made on the custom TEM chip in preparation for measuring conductivity. The whole process will be performed on a Si/SiN_x substrate. Firstly, a

reactive ion etching system will be used to remove the contaminations on the substrate surface and improve photoresist wettability, so that the photoresist will be applied uniformly on spin-coating. The wiring diagram of the conductivity measurement device will be traced with electron beam lithography, and the pattern of electrode formation will be obtained by removing the unwanted photoresist with an organic solvent. Afterward, Cr/Au will be vaporized using an electron beam evaporation system to obtain electrodes with the pattern. Finally, a focused ion beam will be used to create inter-electrode nano-gaps by cutting the electrodes with ion beams.

(1) Cleaning

Hold the non-window part of the Si/SiN_x chip with reverse tweezers and immerse it vertically in Acetone solution, Isopropyl alcohol solution (IPA), and deionized water (DIW) for three minutes sequentially to clean the surface of the chip. The TEM chip after cleaning is shown as Figure 2.5.

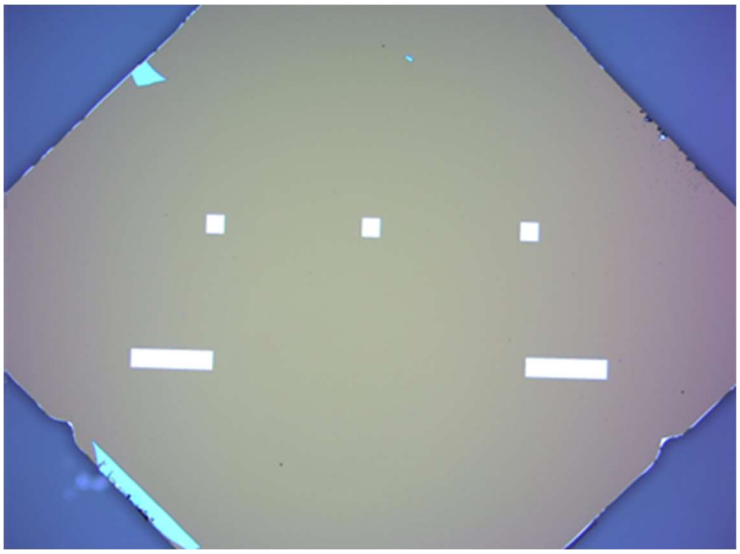

Figure 2.6 The TEM chip after cleaning.

(2) Fixation of TEM chip on aluminum plate

An aluminum (Al) plate is designed to fix the TEM chip for protection, as shown in Figure 2.6. The TEM chip is small, with dimensions of 2.6×2.6 mm, so it is difficult to place the chip on the spin coating stage appropriately. And the TEM chip consists of a Si substrate with a thickness of 200μm and a SiN_x film with a thickness of 50nm covered on the Si substrate. To prevent the SiN_x film from being damaged. a through hole was made in the aluminum plate. Firstly, the TEM chip is stuck to the Al plate with poly (methyl methacrylate) (PMMA), which is then heated on the hot plate at 180 °C for 5 minutes.

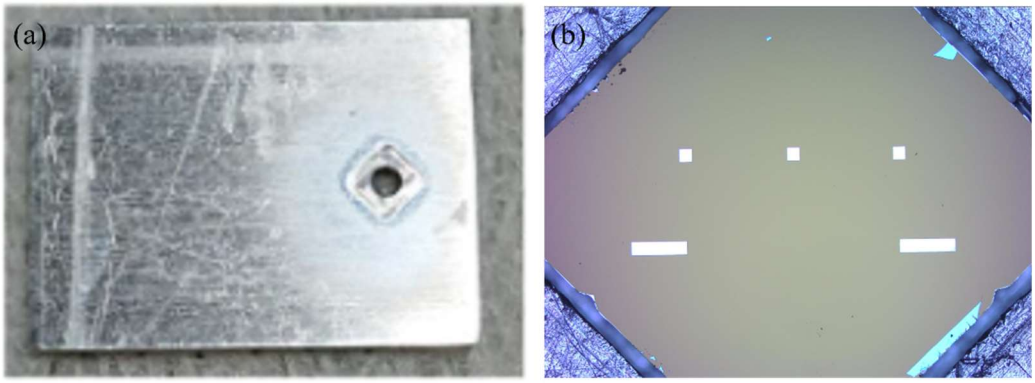

Figure 2.7 (a) Designed aluminum Plate. (b) The fixed TEM chip on the Al plate

(3) Reactive ion etching

Place the Al plate fixed with the TEM chip in the reactive ion etching system (RIE) to clean the surface of the TEM chip. We use the RIE-10NR fabricated by SAMCO Company as shown in Figure2.7. The recipe for the cleaning process is shown on Table 2.1.

Figure 2.8 The reactive ion etching system

Table 2.1 The parameters for the reactive ion etching

Gas	Flow	Radio Frequency Power	Time	Pressure
O_2	10sccm	100 W	4 min	4.0 Pa

(5) Resist coating

Thin layers of methyl methacrylate (MMA) and polymethyl methacrylate (PMMA) are spin-coated onto the TEM chip to form a bilayer electron beam resist system. The setup and coated chip are shown in Figures 2.7, respectively. Coating parameters for MMA and PMMA are summarized in Tables 2.2 and 2.3.

Both MMA and PMMA are positive electron beam resists, meaning they are degraded and become soluble in developer upon electron beam exposure. In this bilayer system, MMA is used as the bottom layer because it is more sensitive and dissolves faster than PMMA. When exposed to the same electron beam dose, the MMA layer develops more quickly than the PMMA layer, producing a inverted stair-like structure.

This undercut geometry is important for lift-off processes. It prevents metal from sticking to the sidewalls of the resist, ensuring that the deposited metal makes good contact only with the substrate and not with the resist sidewalls. As a result, the metal electrodes formed after lift-off have sharper edges and cleaner boundaries, which is critical for reliable electrical contact in nanoscale devices.

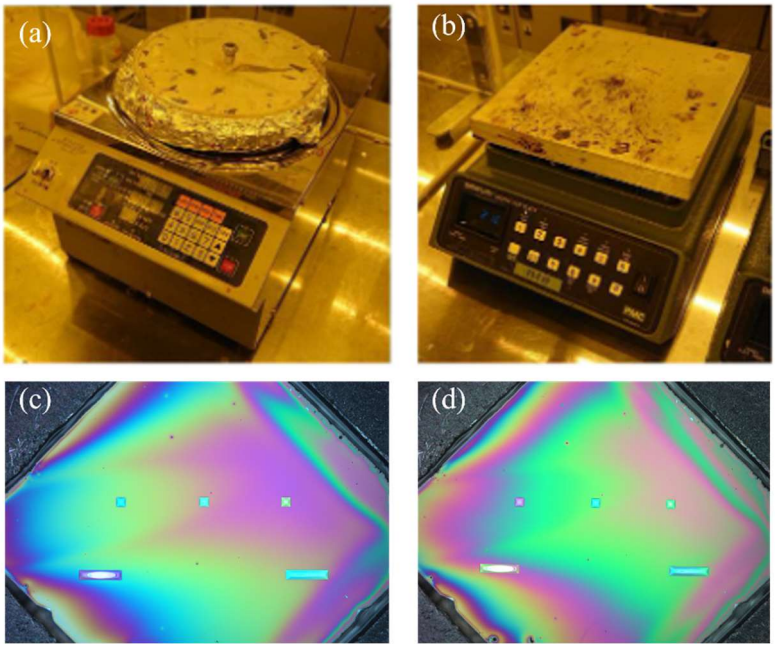

Figure 2.9 (a) The spin coater. (b) The heating stage. (c) The TEM chip after coating MMA. (d) The TEM chip after coating PMMA.

Table 2.2 The parameters for MMA coating

Program Step	**Time [sec]**	**Rotating Speed [rpm]**
00	2	slope
01	5	500
02	2	slope
03	60	2000
04	2	slope
05	End	End

Table 2.3 The parameters for PMMA coating

Program Step	Time [sec]	Rotating Speed [rpm]
00	2	slope
01	5	500
02	2	slope
03	60	4000
04	2	slope
05	End	End

(6) Electron beam lithography and development

Electron Beam Lithography (EBL) can design electrode shapes. We use the ELS-7500 fabricated by ELIONIX Company, as shown in Figure 2.8, and the exposure dose is 300 μC/cm2 with a 1nA current. Then, the developer can dissolve away the exposed regions and leave behind the designed pattern. The process is shown in Table 2.4. The TEM chip before and after development is shown in Figure 2.8.

Figure 2.10 The electron beam lithography system

Table 2.4 The parameters for development

Step	Solution	Time
1	MIBK : IPA = 1 : 3	2 min
2	MIBK : IPA = 1 : 1	10 s
3	IPA	45 s

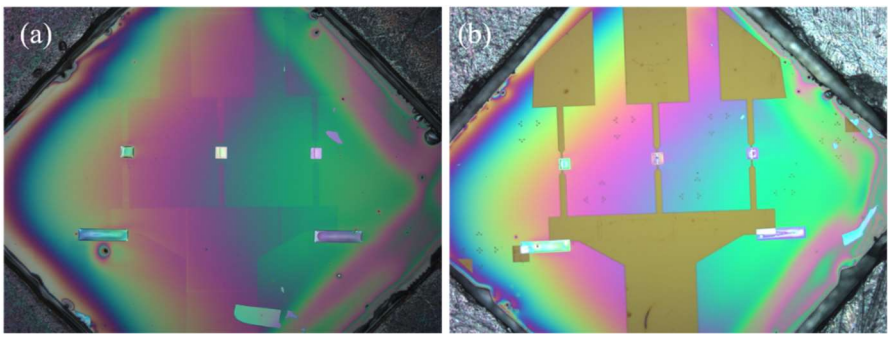

Figure 2.11 (a) The designed electrode pattern before development. (b) The TEM chip after development.

(7) Electron beam deposition

The Electron Beam Evaporation system can deposit high-quality metal films. We use MUE-ECO-EB fabricated by ULVAC Company, as shown in Figure 2.10. Firstly, the chromium (Cr) with a thickness of 5nm is deposited as a bonding agent between gold (Au) and the TEM surface. Afterward, the Au with a thickness of 40 nm is deposited over the Cr layer. The TEM chip after deposition is shown in Figure 2.11.

Figure 2.12 The electron beam evaporation system.

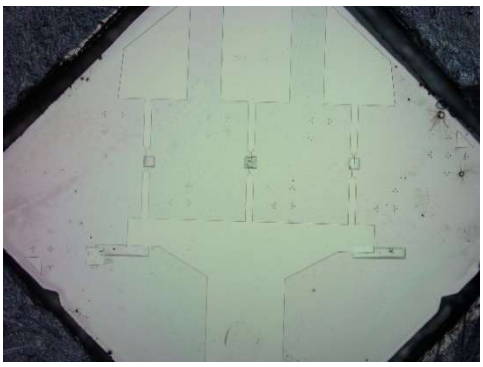

Figure2.13 TEM chip after deposition of 5 nm Cr and 40 nm Au.

In this study, Cr was used as an adhesion layer, and several metals were considered for the main electrode, including gold (Au), platinum (Pt), titanium (Ti), and indium (In). The choice of electrode material was based on both material properties and practical fabrication limitations.

Ti ($\Phi_M \approx 4.3\ eV$) and In ($\Phi_M \approx 4.1\ eV$) have relatively low work functions, which in principle can reduce the Schottky barrier for electron injection in n-type MoS_2. However, both materials are prone to oxidation and are less chemically stable in ambient conditions. In particular, In has a low melting point (~157 °C), making it unsuitable for post-fabrication annealing processes that are essential for removing polymer residues. Ti, while mechanically robust, has a significantly higher resistivity than Au and also tends to form a surface oxide layer, which can degrade electrical contact quality.

Pt is more chemically stable and has a high work function ($\Phi_M \approx 5.6\ eV$), but it presents challenges in both deposition and patterning. Our metal films were deposited using a MUE-ECO-EB electron beam evaporator, which offers limited precision in controlling deposition rate. Under these conditions, Pt tends to deposit much more quickly than Au, making it difficult to control the film thickness and uniformity. Although Pt films are less prone to bubble formation during deposition, they show higher surface and edge roughness after the lift-off process.

To compare film quality, we deposited Cr/Au and Cr/Pt electrodes on identical TEM chips using the same lithography parameters. The resulting electrode surfaces were characterized using AFM, as shown in Figure 2.12. The root mean square (RMS) roughness of Pt electrodes was significantly higher than that of Au, as shown in Table 2.5. Thus, Cr/Au electrodes offer better process stability and surface quality under our current fabrication conditions.

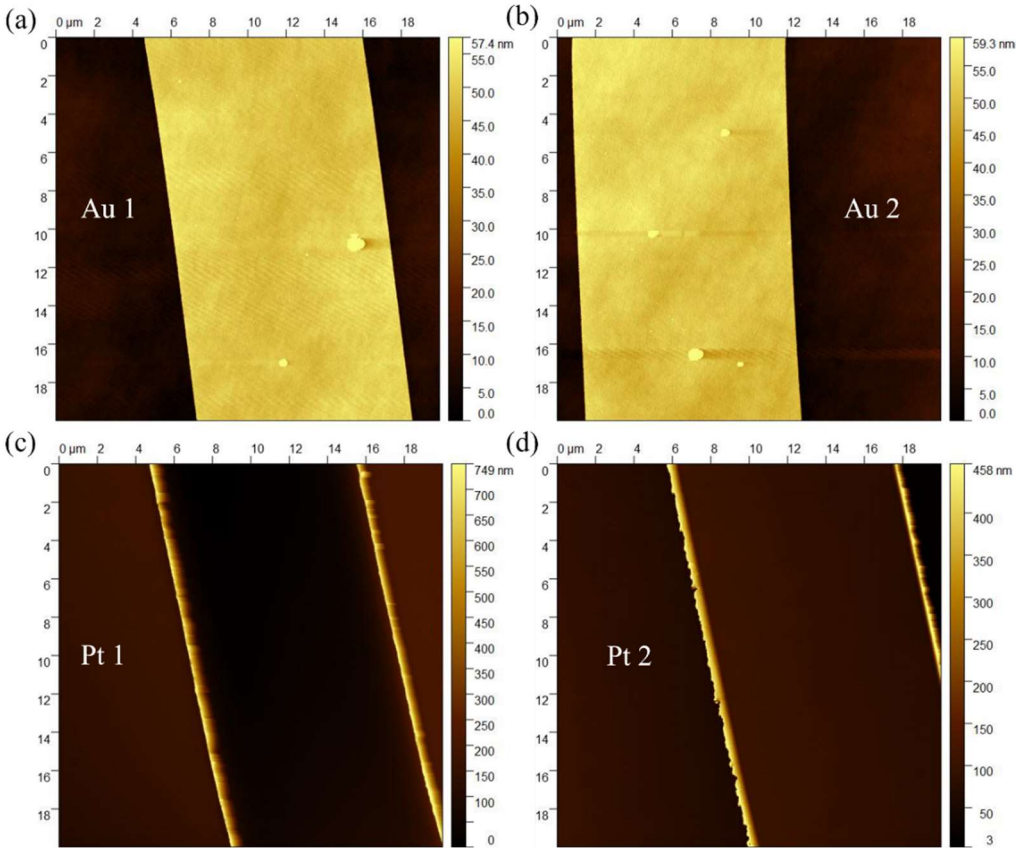

Figure 2.14 Atomic force microscopy (AFM) images of electrode surfaces. (a) and (b) show Au electrodes; (c) and (d) show Pt electrodes.

Table 0.5 The RMS roughness of Au and Pt parameters for development

Sample	Au 1	Au 2	Pt 1	Pt 2
RMS Roughness	25.67nm	24.53nm	113.5nm	52.90nm

(8) Lift-off

N-methyl-2-pyrrolidone (NMP) is used to dissolve the MMA/PMMA resist layers, leaving behind the metal electrodes, as shown in Figure 2.13. After lift-off, the TEM chip is rinsed in isopropyl alcohol (IPA) and dried with a nitrogen gun.

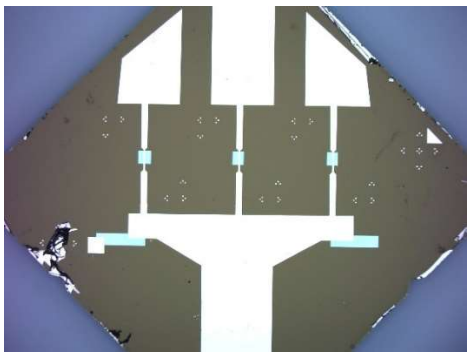

Figure 2.15 The TEM chip after lift-off process.

Reference

[1] Novoselov, K. S.; Geim, A. K.; Morozov, S. V.; Jiang, D.; Zhang, Y.; Dubonos, S. V.; Grigorieva, I. V.; Firsov, A. A. Electric Field Effect in Atomically Thin Carbon Films. Science 2004, 306 (5696), 666–669. https://doi.org/10.1126/science.1102896.

[2] Li, H.; Zhang, Q.; Yap, C. C. R.; Tay, B. K.; Edwin, T. H. T.; Olivier, A.; Baillargeat, D. From Bulk to Monolayer MoS_2: Evolution of Raman Scattering. Adv. Funct. Mater. 2012, 22 (7), 1385–1390. https://doi.org/10.1002/adfm.201102111.

[3] Li, H.; Wu, J.; Huang, X.; Lu, G.; Yang, J.; Lu, X.; Xiong, Q.; Zhang, H. Rapid and Reliable Thickness Identification of Two-Dimensional Nanosheets Using Optical Microscopy. ACS Nano 2013, 7 (11), 10344–10353. https://doi.org/10.1021/nn4047474.

[4] Puebla, S.; Li, H.; Zhang, H.; Castellanos-Gomez, A. Apparent Colors of 2D Materials. Adv. Photonics Res. 2022, 3 (4), 2100221. https://doi.org/10.1002/adpr.202100221.

[5] Puebla, S.; Mariscal-Jiménez, A.; Galán, R. S.; Munuera, C.; Castellanos-Gomez, A. Optical-Based Thickness Measurement of MoO3 Nanosheets. Nanomaterials 2020, 10 (7), 1272. https://doi.org/10.3390/nano10071272.

[6] Frisenda, R.; Niu, Y.; Gant, P.; Molina-Mendoza, A. J.; Schmidt, R.; Bratschitsch, R.;

Liu, J.; Fu, L.; Dumcenco, D.; Kis, A.; Lara, D. P. D.; Castellanos-Gomez, A. Micro-Reflectance and Transmittance Spectroscopy: A Versatile and Powerful Tool to Characterize 2D Materials. J. Phys. Appl. Phys. 2017, 50 (7), 074002. https://doi.org/10.1088/1361-6463/aa5256.

[7] Liu, C.; Zhang, J.; Muruganathan, M.; Mizuta, H.; Oshima, Y.; Zhang, X. Origin of Nonlinear Current-Voltage Curves for Suspended Zigzag Edge Graphene Nanoribbons. Carbon 2020, 165, 476–483. https://doi.org/10.1016/j.carbon.2020.05.010.

[8] Liu, C.; Zhang, J.; Zhang, X.; Muruganathan, M.; Mizuta, H.; Oshima, Y. *in-situ* Electrical Conductance Measurement of Suspended Ultra-Narrow Graphene Nanoribbons Observed via Transmission Electron Microscopy. Nanotechnology 2020, 32 (2), 025710. https://doi.org/10.1088/1361-6528/abbca7.

[9] Liu, C.; Zhang, J.; Ganesh Ramaraj, S.; Zhang, X.; Muruganathan, M.; Mizuta, H.; Oshima, Y. Current Effect on Suspended Graphene Nanoribbon Studied Using in–Situ Transmission Electron Microscopy. Appl. Surf. Sci. 2022, 573, 151563. https://doi.org/10.1016/j.apsusc.2021.151563.

Chapter 3 PPC-based all dry transfer method for 2D device fabrication

Introduction

This chapter presents the deterministic placement of 2D flakes for device fabrication. In Chapter 3.1, we make a comprehensive description of the recently developed transfer methods of 2D materials. In Chapter 3.2, we introduce the advantage and detailed processes of PPC-based all dry transfer method to transfer few layer MoS_2 flakes. In Chapter 3.3, the fabricated MoS_2 devices were characterized by TEM.

3.1 Comparison of different method

One of the key limitations of in situ experiments of 2D materials is the difficulty in manipulating the sample from the growth substrate to the in situ TEM testing stage. The transfer of MoS_2 flakes is the crucial step for the manufacture of two terminal MoS_2 devices. Previously, C. Liu et al. have established the wet transfer process for GNR devices.[1] However, the capillary forces involved during the wet transfer procedure may affect the edge structure of the MoS_2 monolayer, which can be avoided in all-dry transfer instead.

The all-dry transfer method using PDMS stamp, which is much more convenient than wet transfer, is often used to fabricate 2D heterostructures.[2] Due to the viscoelasticity, the PDMS stamp behaves as an elastic solid while attaching, but it can slowly flow over a while if maintaining contact. The pick-up process depends on the viscosity of PDMS, and the peel-off process needs to be slow to ensure the flakes can adhere to the targeted area preferentially.

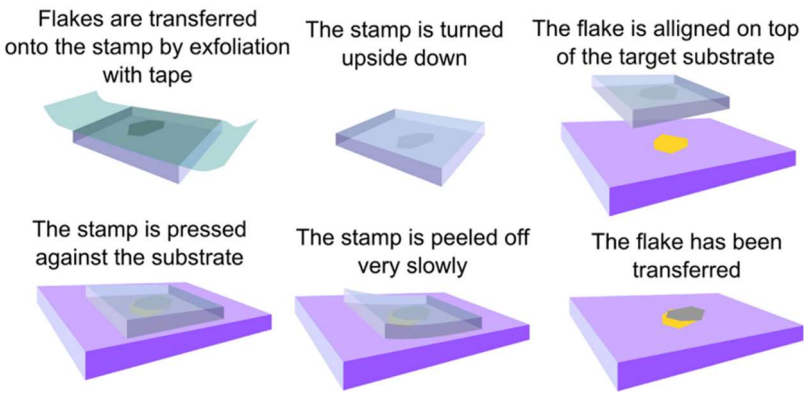

Figure 3.1 The process of PDMS-based all-dry transfer.[2]

However, when it comes to fabricating suspended 2D nanoribbons, the success ratio is not satisfactory enough. Fukumoto et al. have fabricated suspended GaSe nanoribbon using a PDMS-based all-dry transfer method.[3] In his challenge, it was quite hard to transfer very thin GaSe flake on the TEM chip. The viscosity of PDMS is as weak as 1.0 cSt at room temperature, so picking up flakes from the substrate using a PDMS stamp is difficult, and the size and number of layers of 2D material cannot be controlled. And once the pick-up process is finished, it is difficult to release the flakes from the PDMS stamp to the targeted chip without breaking the suspended SiN film, because the viscosity of PDMS is stable with its high glass transition temperature of around 120°C.

To control the control pick-up and peel-off process, it has been reported that it is effective to use the glass transition of polymers. The polymer has high viscosity because

of quenching the molecular motion at lower temperature than the glass phase transition temperature, while it has low viscosity at higher temperature than one. It means that, below the transition temperature, the interface with the target 2D material will not adhere well, making it easier to separate from the stamp. On the other hand, the opposite occurs above the transition temperature. In this study, we found that the most suitable polymer for the transfer stamp was PPC instead of PDMS. The PPC has strong viscosity of 2.5 cSt at room temperature, which is more than twice that of the PDMS. The high viscosity ensures that the PPC can always pick up the 2D flakes on the Si/SiO_2 substrate, and can control the size and number of layers of the targeted flake. As for the peel-off process, the viscosity of PPC becomes very weak at higher temperatures due to its thermoplastic property, so less pressure can be used to release the flake from the PPC stamp to the desired area, avoiding the SiN film cracking. Here is the device comparison of PDMS-based and PPC-based all-dry transfer, as shown in Figure 3.2. The flakes transferred onto electrodes by PDMS is large, thick, and non-uniform in thickness. On the contrary, the flakes transferred by PPC are small, thin, and uniform. Thus, the PPC-based all-dry transfer method is more possible to make high-quality suspended devices.

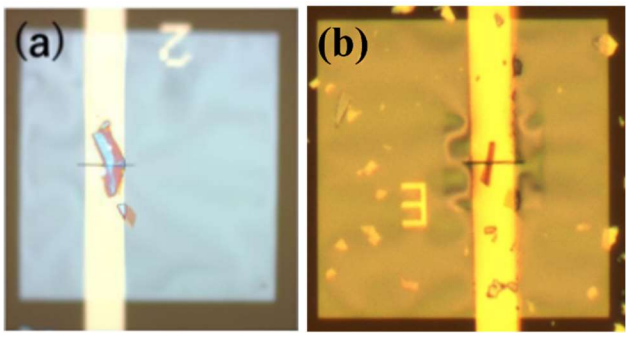

Figure 3.2 (a) GaSe flake transferred by PDMS stamp.[3] (b)MoS_2 flake transferred by PPC stamp

3.2 The process of PPC-based all-dry transfer method

As shown in Figure 3.3, firstly, the stamp of PPC/PDMS fabricated with a spinning coating will be fixed on a moving stage. Then, the temperature of the SiO_2 substrate will be raised to 60℃ for stamp contacting. Next, the temperature will be decreased to 40℃ to shrink the PPC/PDMS stamp and pick up the targeted flake. Afterward, fixing the measuring SiN/Si chip on the heating stage and increasing the temperature to 120℃, since the viscosity of the PPC weakens, the stamp will release the MoS_2 flake and put it down to the determined position on the electrode. The specific explanation about this method is as follows.

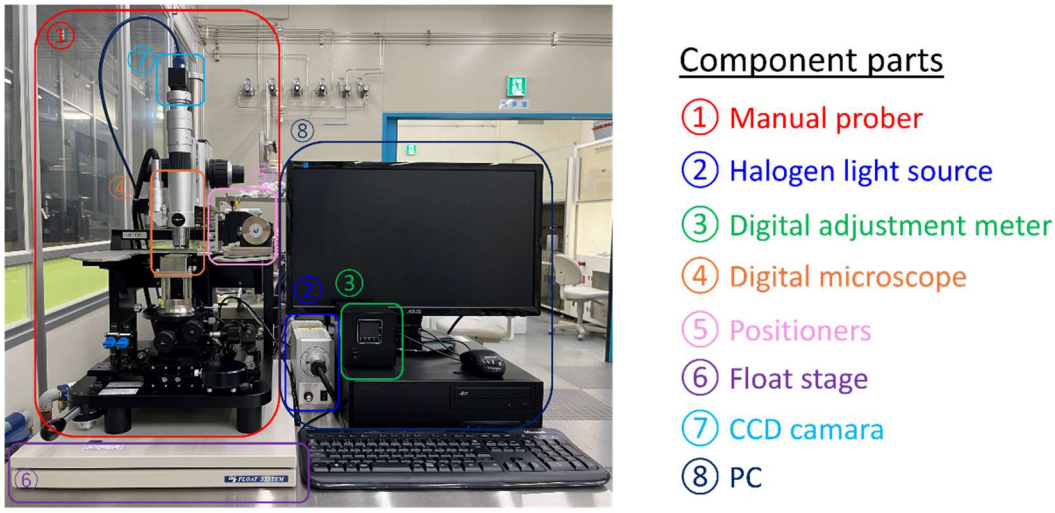

Figure 3.3 Equipment used for PPC-based dry transfer

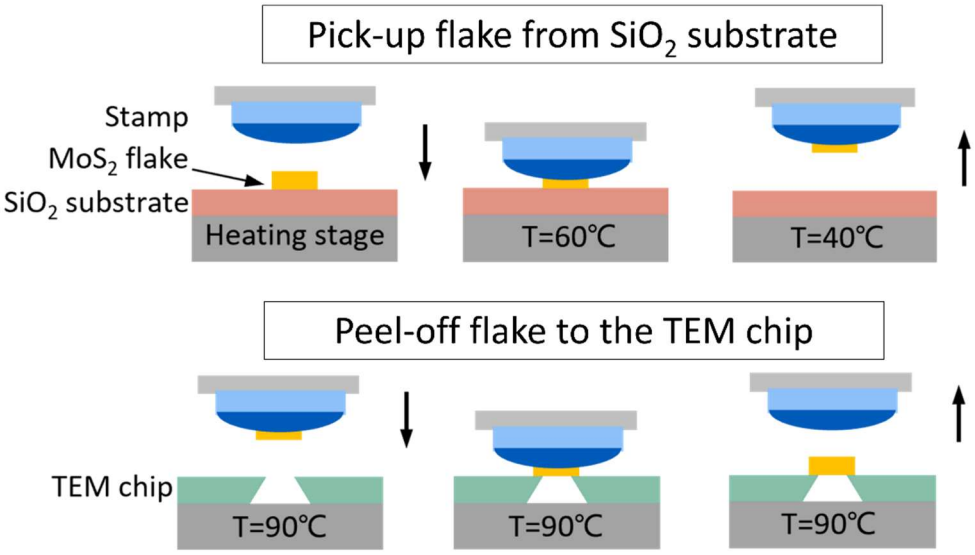

Figure 3.4 The temperature control transfer process by PPC stamp

(1) Sample preparation

Firstly, fix the SiO_2 substrate on the heating table with copper tape and heat it to 110 ºC. Tear the 3M adhesive tape with 2D material several times, stick it on the SiO_2 substrate,

wait for 2min, and gently press it with a cotton swab. Lower the temperature to 80 ºC, then quickly peel off the adhesive tape, and observe the adhesion of 2D materials on the SiO_2 substrate. Repeat the above steps if necessary, then choose the thinner flakes with blue color as targeted flakes on the substrate shown in Figure 3.4.

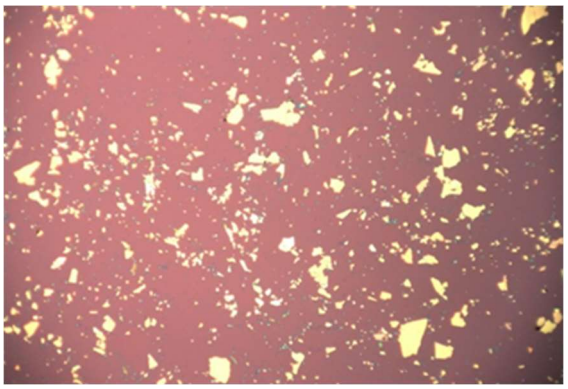

Figure 3.5 The MoS_2 flakes exfoliated on the Si /Si substrate

(2) Stamp fabrication

Firstly, cut about 1mm square PDMS with a cutter and stick the PDMS on the cover glass. Then, treating the bare side of PDMS with O_2 plasma to prevent PPC from falling off suddenly. Afterward, spin coating liquid PPC on the PDMS using 8000 rpm speed, and bake it at bake at 110ºC for 5 minutes.

(3) Pick-up process

First, the temperature was adjusted to 60℃ suitable for contact. Here, PPC is glass and becomes soft so that it can fully contact flakes. Next, to achieve smooth shrinkage of the contact area, the temperature will be decreased from 60℃ to 40℃. Abrupt shrinkage

of the contact area can damage the flakes. Afterward, the MoS_2 flake will be picked up from the surface of the SiO_2 substrate.

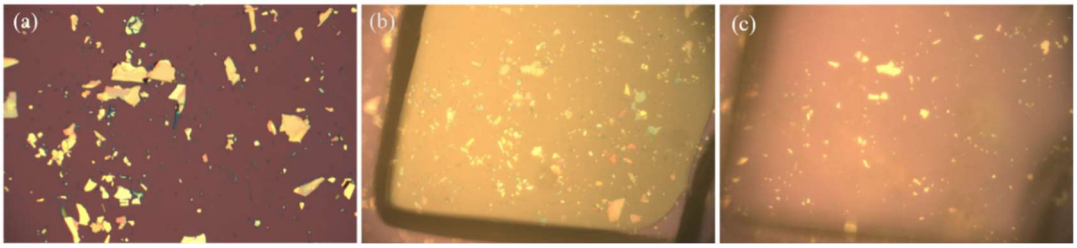

Figure 3.6 (a) MoS_2 flakes on the substrate. (b) PPC/PDMS stamp contact the substrate. (c) Flakes were picked up on the stamp.

(4) Peel-off process

First, the temperature was raised to 90℃ and kept for 5 minutes. The viscosity of PPC was decreased and can release the flake at 90℃. Alignment between the stamp and the substrate was necessary until the center of the stamp was able to touch the substrate. After contacting, flakes were slowly peeled off from the PPC stamp. Finally, the MoS_2 flake was transferred to the gap of the electrode.

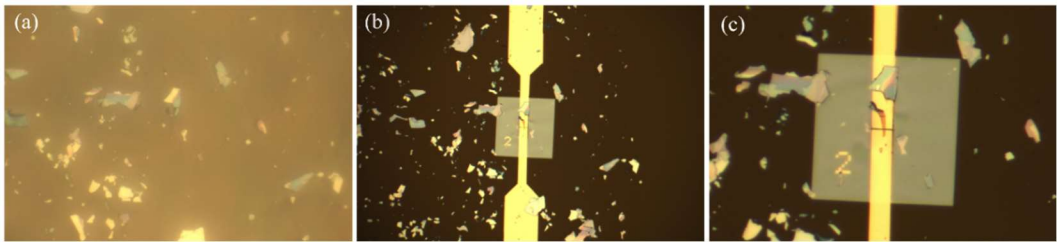

Figure 3.7 (a) Align the MoS_2 flake with the gap of electrode. (b) MoS_2 is released from the stamp. (c) MoS_2 flake suspends on the gap of electrode.

3.3 The characterization of transferred MoS_2 flakes

In this research, four suspended MoS_2 nanoribbon devices are fabricated and characterized by TEM. According to the optical contrast, the layer numbers of these MoS_2 flakes are estimated to be 15, 7, 10, and 4 layers respectively. The TEM can be used to check the quality of these MoS_2 devices. The images in our research are acquired by JEM-ARM 200F under 120 kV. As shown in Figure 3.7, the surface and the edge of the sample are clean, only a small amount of contamination is present at the edges of the sample.

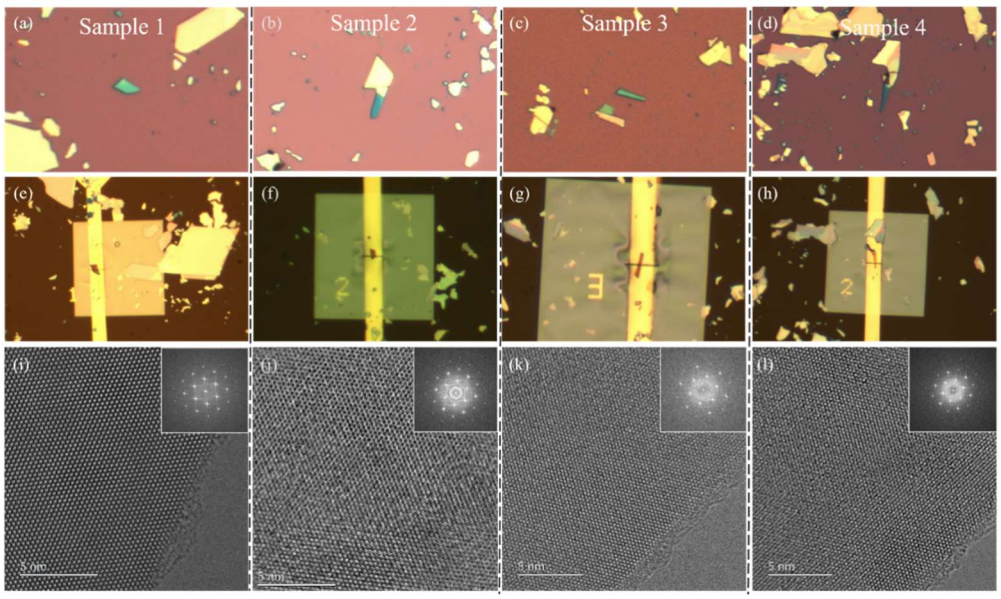

Figure 3.8 (a-d) The MoS_2 flakes before transfer. (e-f) The MoS_2 nanoribbon devices made by flakes in (a-d). (i-l) The TEM high resolution images of the MoS_2 nanoribbon edge areas and corresponding FFT.

Reference

[1] Liu, C.; Zhang, J.; Zhang, X.; Muruganathan, M.; Mizuta, H.; Oshima, Y. In-Situ Electrical Conductance Measurement of Suspended Ultra-Narrow Graphene Nanoribbons Observed via Transmission Electron Microscopy. Nanotechnology 2020, 32 (2), 025710. https://doi.org/10.1088/1361-6528/abbca7.

[2] Castellanos-Gomez, A.; Buscema, M.; Molenaar, R.; Singh, V.; Janssen, L.; Zant, H. S. J. van der; Steele, G. A. Deterministic Transfer of Two-Dimensional Materials by All-Dry Viscoelastic Stamping. *2D Mater.* **2014**, *1* (1), 011002. https://doi.org/10.1088/2053-1583/1/1/011002.

[3] Fukumoto, K. TEM *in-situ* Observation of Electrical Conductivity of GaSe Nanoribbons.

Chapter 4 Cleaning of MoS_2 Devices

Introduction

This chapter presents the surface cleaning strategy developed for MoS_2 devices used in *in-situ* TEM studies. In Chapter 4.1, we describe the strict cleanliness requirements for electron-transparent samples, with emphasis on the challenges posed by contamination in high-resolution and beam-sensitive measurements. In Chapter 4.2, we outline the typical sources of contamination during MoS_2 device fabrication, including polymer residues and transfer-related artifacts. In Chapter 4.3, we evaluate a series of conventional cleaning techniques, discuss their limitations for MoS_2, and summarize experimental attempts. In Chapter 4.4, we introduce Ar/H_2 atmosphere annealing as a gentle and effective cleaning approach, and demonstrate its success in enabling atomic-resolution imaging after treatment.

4.1 The Importance of TEM Sample Cleanliness

4.1.1 Cleanliness Requirements for TEM Samples

The TEM observation demands exceptionally clean samples due to its outstanding spatial resolution and sensitivity to atomic-scale features.[1,2] The specimen contamination is a severe problem for the observation. This requirement becomes even more critical in *in-situ* experiments, where dynamic processes such as electrical switching, charge modulation, or structural transitions are monitored in real time under electron beam exposure.[3]

Common contaminants including polymer residues, hydrocarbons, and adsorbed moisture layers undergo unpredictable evolution under electron beam irradiation.[4] These species readily undergo radiolysis and cross-linking, often forming amorphous carbon clusters that progressively grow during STEM observation. Such beam-induced transformations not only degrade image contrast and resolution but also create spurious electrical pathways in *in-situ* device measurements.

Polymer residues trapped at MoS_2-electrode or MoS_2-substrate interfaces can affect the contact, distorting the intrinsic transport behavior of devices. Localized charging or heating effects from electron beam interaction with residual contaminants can lead to parasitic currents, which disturbing the investigation of electrostatic gating or dielectric

charging. For *in-situ* STEM measurements of 2D materials like MoS_2, achieving high surface cleanliness is fundamental to experimental validity. Minimizing contamination is essential for drawing accurate conclusions about charge transport, interface dynamics, and gating mechanisms.

4.1.2 Origins of Contaminants in this study

Despite meticulous fabrication protocols, surface contamination is an almost inevitable consequence of nanodevice processing, particularly in the case of 2D materials such as MoS_2. Various stages of device assembly introduce distinct classes of residues, many of which persist through standard cleaning routines and become problematic under the high-energy electron beam of a TEM. Understanding the origins of these contaminants is essential for developing effective removal strategies.

One of the earliest sources of contamination stems from the exfoliation process. Mechanical exfoliation using adhesive tapes can introduce organic particles, adhesive residues, or oxidation byproducts onto the MoS_2 surface. Even brief ambient exposure during flake selection or storage can lead to physiosorbed water layers or hydrocarbon films, which may not be entirely eliminated by mild heating or solvent rinsing.

A second kind of contaminants originates from the polymeric materials used during the device fabrication process, which is more persistent. In particular, PPC or PDMS

stamp are widely employed as intermediate carriers for positioning exfoliated flakes onto target substrates. While these polymers enable precise alignment and mechanical protection, they often leave behind molecular residues even after nominal solvent cleaning. These residues tend to accumulate at critical locations, such as the MoS_2-electrode interface or the suspended region of the flake, where they are difficult to access or remove post-fabrication.

Additional contamination may arise during lithographic patterning and metal deposition. For instance, resist residues, developer traces, or outgassing from electron-beam exposure can adsorb onto the flake surface. Furthermore, even in the absence of active processing steps, prolonged exposure to laboratory air can lead to the adsorption of airborne hydrocarbons or adventitious carbon, which become increasingly problematic during *in-situ* imaging.

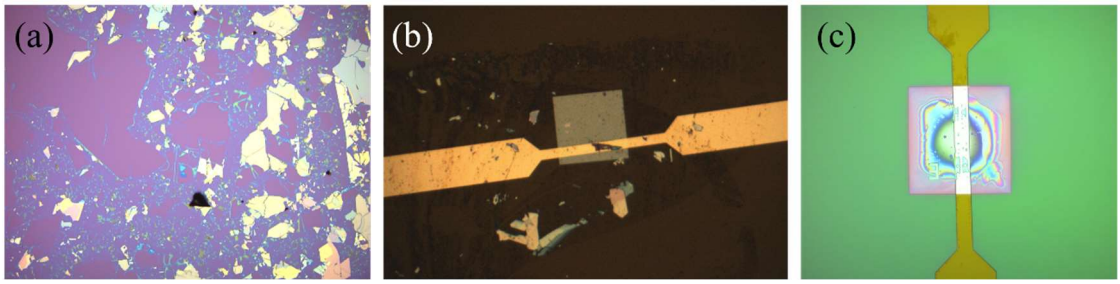

Figure 4. 1 (a) Adhesive residue of tape. (b) PPC polymer residue after transfer. (c) PMMA photoresist residue during electrode fabrication.

These contamination sources pose particular challenges in *in-situ* STEM studies. Therefore, identifying and eliminating these contamination sources is essential prior to any *in-situ* electrical or spectroscopic experiment. In the following section, we evaluate conventional cleaning strategies and explain why many of them fall short when applied to sensitive MoS_2 devices.

4.2 Different methods for 2D material cleaning

To maintaining a clean sample surface, numerous cleaning strategies have been developed to mitigate surface contamination, especially polymer residues and hydrocarbon buildup. These methods vary in their physical principles, effectiveness, and compatibility with sensitive materials.

O_2 plasma cleaning is a fast and widely adopted technique for removing hydrocarbon and carbonaceous contaminants from TEM grids and surfaces.[5–7] However, this method is generally unsuitable for MoS_2 and other 2D sulfide materials, as it can induce undesirable chemical reactions. Energetic plasma species can remove surface sulfur atoms or introduce oxygen-containing functional groups, thereby degrading the intrinsic properties and structural integrity of the flake.

Beam showering is often used under STEM mode. It irradiates a very large area of specimen with a high electron flux so that hydrocarbons which might otherwise migrate

are cracked and form an extremely thin layer of immobile carbon. This showered area can then be examined in detail without contamination occurring, at least in the short-term.[8,9] The shortcoming is that beam showering area is inherently limited in scope. It only stabilizes existing amorphous contaminants and fix them to the substrate surface, thereby preventing their migration and accumulation under focused beam exposure. It does not actively remove residues from the MoS_2 surface and is ineffective for pre-imaging cleaning of transferred samples.

UV/ozone cleaning generates reactive oxygen species that can chemically break down organic residues, and has shown good performance in several microscopy contexts.[2,10] However, due to equipment limitations, this method could not be implemented in our experimental setup.

In addition to reviewing these reported methods, we also attempted several cleaning techniques and evaluated them in terms of their effectiveness in removing transfer-related residues and their compatibility with MoS_2 under *in-situ* STEM conditions. As a first approach, we tested low-temperature vacuum baking using the internal heating system of the TEM holder pumping workstation. However, since the temperature inside the vacuum chamber could not be precisely controlled or monitored, the heating process led to severe structural degradation of the MoS_2 flake. After baking, numerous holes and amorphous

clusters were observed on the flake surface, as shown in Figure 4.2, indicating that even uncontrolled heating can cause irreversible damage to MoS_2 structures.

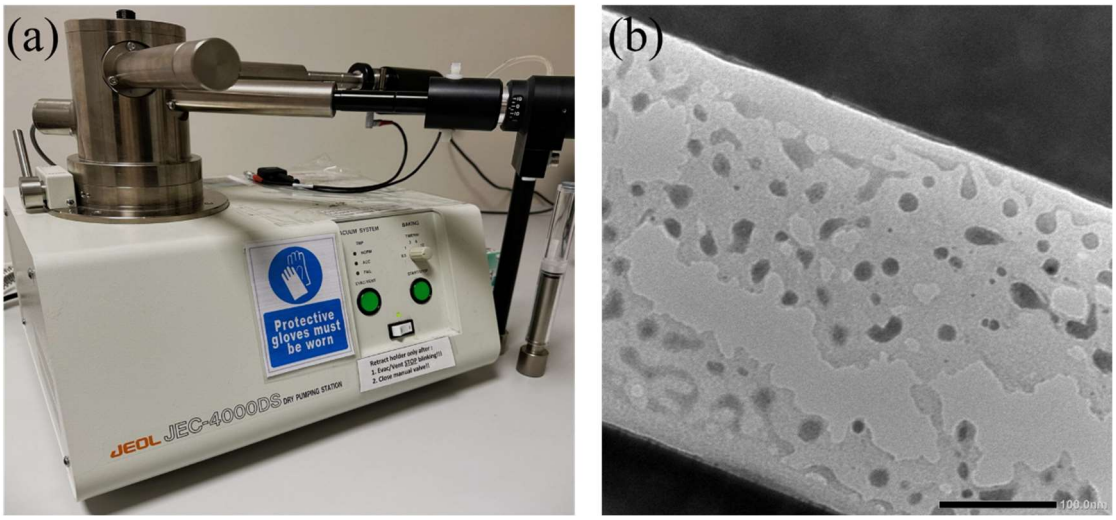

Figure 4.2 (a) TEM holder dry pumping station. (b) Low magnification TEM image of MoS_2 flake after baking.

Then, we employed halogen point heating under high vacuum conditions to promote desorption of surface contaminants, as shown in Figure 4.2 (a) and (b). The system was equipped with a turbomolecular pump (TMP), allowing sample heating in a vacuum environment of approximately 10^{-5} Pa. The sample was heated continuously for three hours.

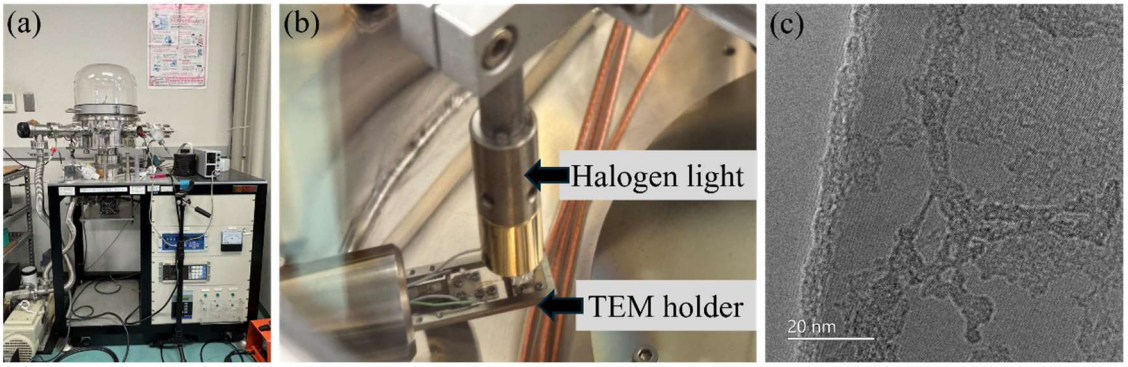

Figure 4.3 (a) Photo of the custom-built halogen lamp vacuum heating system equipped with a TMP. (b) The relative positioning of the halogen light source and the TEM holder during heating. (c) Low magnification TEM image of MoS_2 flake after halogen point heating.

The low magnification TEM image revealed the presence of residual surface films with characteristic cross-linked morphology, as shown Figure 4(c). These residues were likely the result of incomplete decomposition or thermally-induced polymerization of transfer polymers. When examined under STEM, these residual layers exhibited beam-induced contamination buildup. Instead of being removed, the residues dynamically accumulated during imaging, making it impossible to acquire stable atomic-resolution images due to the progressive darkening and contrast loss. This result suggests that, despite the high vacuum, uncontrolled halogen heating is insufficient for removing beam-sensitive contaminants and may even promote their cross-linking under sub-optimal conditions.

In-situ current annealing, based on Joule heating, is proved to be effective in graphene nanoribbon (GNR) cleaning.[11] It involves applying a gradually increasing source-drain

bias across the device, inducing a large current density through the active channel. This current generates localized heating and effectively removes adsorbed contaminants such as polymer residues or hydrocarbon films.

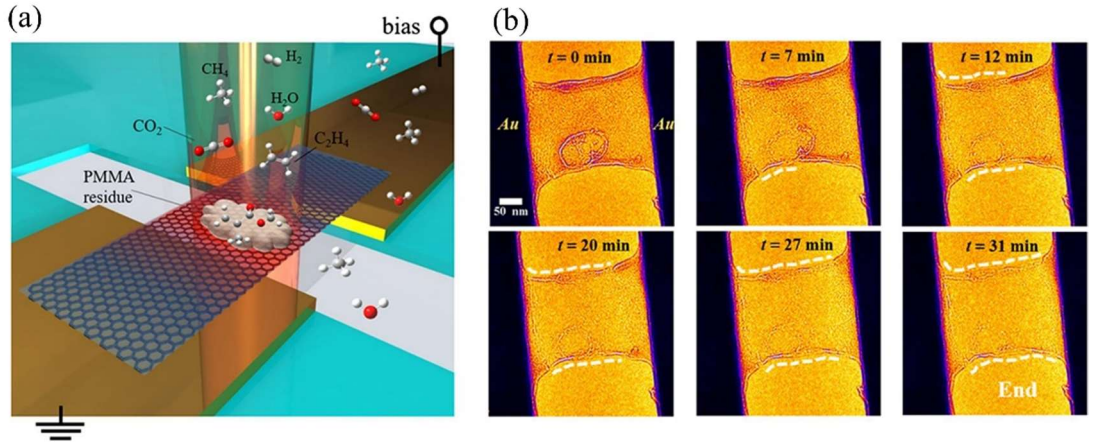

Figure 4.4 (a) 3D schematic of the current annealing process, which shows the removal of PMMA residues from the surface of GNR when applying a high bias voltage. (b) TEM images for GNR during current annealing captured at different time intervals.[11]

However, when applied to MoS_2 devices, this method proves problematic for several reasons. First, the uncontrolled current-induced heating can easily raise local temperatures above 800 K, which significantly exceeds the thermal stability limit of MoS_2. Such high temperatures can induce sulfur desorption, structural breakdown of the lattice. Besides, we observed that once thermal damage occurred, residual amorphous contamination on the MoS_2 surface often transformed into nanoribbon-like structures. These cross-linked residues became stable even under elevated current conditions,

making further annealing ineffective. Instead of cleaning the surface, the process led to persistent contamination and irreversible degradation of the channel.

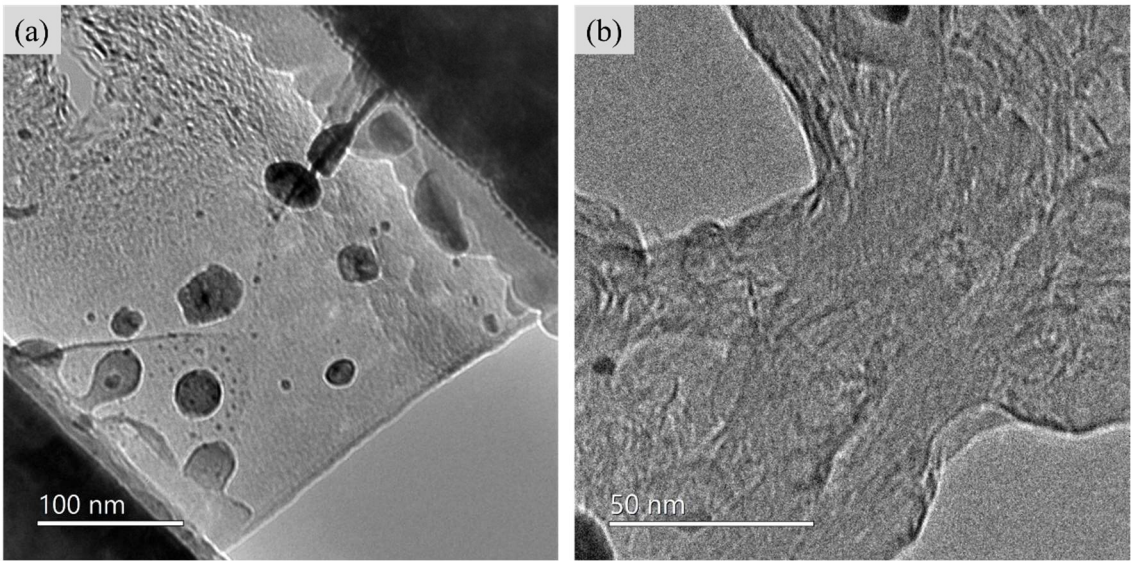

Figure 4.5 (a) Low-magnification TEM image of a MoS_2 flake after *in-situ* current annealing, showing black Mo clusters damage. (b) TEM image of amorphous contamination forming nanoribbon-like structures after MoS_2 flake breakdown.

Together, these results demonstrate that while current annealing is effective for robust and thermally stable materials like graphene, it is not suitable for MoS_2. Its narrow thermal tolerance, combined with the risk of creating electrically conductive residue, makes this method incompatible with the requirements of *in-situ* electrical and imaging studies in 2D chalcogenide systems.

4.3 Ar/H_2 gas atmosphere annealing

Annealing in a reducing gas atmosphere composed of argon and hydrogen (typically Ar/10% H_2) at moderate temperatures (250–300 °C) has emerged as an effective and material-compatible method for cleaning MoS_2-based devices.[12,13] Unlike more aggressive techniques, this method offers sufficient chemical reactivity to break down residual polymers such as PPC and PMMA without compromising the structural integrity of MoS_2.

Hydrogen plays a critical role in decomposing hydrocarbon chains via hydrogenolysis, while the inert argon environment prevents unwanted oxidation. Several studies have demonstrated that this process can efficiently remove common transfer-related residues without altering the crystalline lattice of MoS_2. It preserves the morphology of the flake and maintains clean interfaces, making it suitable for high-resolution STEM imaging and electrical characterization. Moreover, the annealing temperature remains safely below the known transition threshold of MoS_2, avoiding phase transformation or sulfur loss.

In our experiment, we first heated the sample on the hotplate of an infrared lamp furnace (ULVAC VHC-P610CP) and performed annealing in a mixed gas ambient composed of argon and hydrogen ($Ar:H_2$ = 9:1). The schematic of the infrared heating

system is shown in Figure 4.5. The sample was placed on a quartz substrate and positioned at the center of the heating zone to ensure uniform temperature exposure. Gas flow was maintained throughout the process to prevent air ingress and ensure a reducing environment during the entire annealing cycle.

Figure 4.6 Photograph of infrared lamp furnace.

To ensure clean interfaces prior to MoS_2 transfer, we first annealed the bare TEM chip at 300 °C in an Ar/10% H_2 atmosphere for 1 hour. This pre-treatment step was intended to remove residual PMMA and other polymeric contaminants introduced during electrode fabrication. Following the all-dry transfer of MoS_2 flakes onto the treated chips, a second annealing step was conducted at 250 °C for 3 hours under the same reducing gas flow. This lower-temperature annealing was designed to gently remove transfer-related

residues, such as PPC, without risking thermal degradation of the MoS_2.

To evaluate the effectiveness of the overall cleaning procedure, STEM imaging was performed before and after the second annealing step. As shown in Figure 4.6, the sample prior to annealing exhibited substantial amorphous background and contrast fluctuations, which obscured the atomic lattice. After annealing, the contamination was significantly reduced, and the MoS_2 surface appeared much cleaner and more uniform under the electron beam. Most importantly, high-resolution atomic images were successfully obtained post-treatment, confirming that the annealing protocol not only preserved the crystallinity of the flake but also enabled stable, artifact-free observation during *in-situ* measurements.

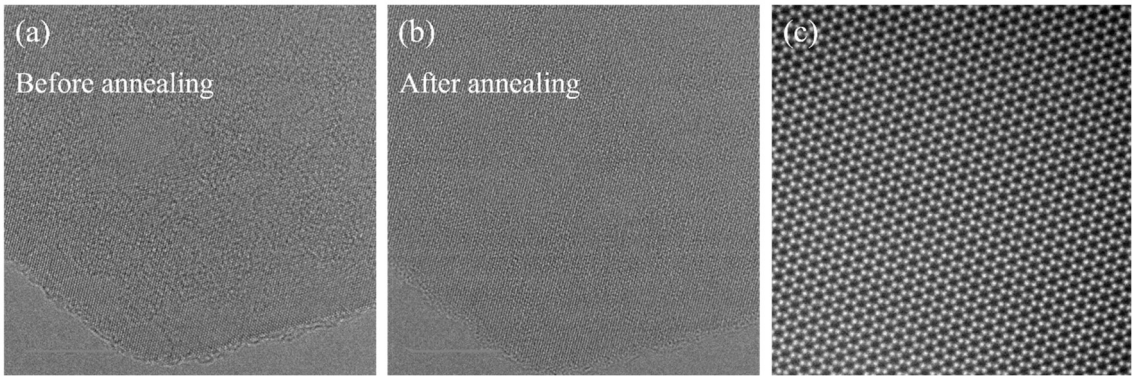

Figure 4.7 (a) TEM image of a MoS_2 flake before annealing, showing notable amorphous contrast due to surface contamination. (b) After annealing at 250 °C for 3 hours in Ar/H_2 atmosphere, the contamination is reduced and lattice fringes become clearer. (c) HAADF image showing the atomic structure of MoS_2 after annealing.

These results verify that moderate-temperature Ar/H_2 annealing provides an effective, non-destructive means of cleaning MoS_2 devices for high-resolution STEM and electrical analysis..

Reference

[1] Egerton, R. F.; Li, P.; Malac, M. Radiation Damage in the TEM and SEM. *Micron* **2004**, *35* (6), 399–409. https://doi.org/10.1016/j.micron.2004.02.003.

[2] Soong, C.; Woo, P.; Hoyle, D. Contamination Cleaning of TEM/SEM Samples with the ZONE Cleaner. *Microsc. Today* **2012**, *20* (6), 44–48. https://doi.org/10.1017/S1551929512000752.

[3] Rummeli, M. H.; Pan, Y.; Zhao, L.; Gao, J.; Ta, H. Q.; Martinez, I. G.; Mendes, R. G.; Gemming, T.; Fu, L.; Bachmatiuk, A.; Liu, Z. In Situ Room Temperature Electron-Beam Driven Graphene Growth from Hydrocarbon Contamination in a Transmission Electron Microscope. *Materials* **2018**, *11* (6), 896. https://doi.org/10.3390/ma11060896.

[4] Hugenschmidt, M.; Adrion, K.; Marx, A.; Müller, E.; Gerthsen, D. Electron-Beam-Induced Carbon Contamination in STEM-in-SEM: Quantification and Mitigation. *Microsc. Microanal.* **2023**, *29* (1), 219–234. https://doi.org/10.1093/micmic/ozac003.

[5] Griffiths, A. J. V.; Walther, T. Quantification of Carbon Contamination under Electron Beam Irradiation in a Scanning Transmission Electron Microscope and Its Suppression by Plasma Cleaning. *J. Phys. Conf. Ser.* **2010**, *241* (1), 012017.

https://doi.org/10.1088/1742-6596/241/1/012017.

[6] Isabell, T. C.; Fischione, P. E.; O'Keefe, C.; Guruz, M. U.; Dravid, V. P. Plasma Cleaning and Its Applications for Electron Microscopy. *Microsc. Microanal.* **1999**, *5* (2), 126–135. https://doi.org/10.1017/S1431927699000094.

[7] McGilvery, C. M.; Goode, A. E.; Shaffer, M. S. P.; McComb, D. W. Contamination of Holey/Lacey Carbon Films in STEM. *Micron* **2012**, *43* (2), 450–455. https://doi.org/10.1016/j.micron.2011.10.026.

[8] Hettler, S.; Dries, M.; Hermann, P.; Obermair, M.; Gerthsen, D.; Malac, M. Carbon Contamination in Scanning Transmission Electron Microscopy and Its Impact on Phase-Plate Applications. *Micron* **2017**, *96*, 38–47. https://doi.org/10.1016/j.micron.2017.02.002.

[9] Dyck, O.; Kim, S.; Kalinin, S. V.; Jesse, S. Mitigating E-Beam-Induced Hydrocarbon Deposition on Graphene for Atomic-Scale Scanning Transmission Electron Microscopy Studies. *J. Vac. Sci. Technol. B* **2017**, *36* (1), 011801. https://doi.org/10.1116/1.5003034.

[10] Hoyle, D.; Malac, M.; Trudeau, M.; Woo, P. UV Treatment of TEM/STEM Samples for Reduced Hydrocarbon Contamination. *Microsc. Microanal.* **2011**, *17* (S2), 1026–1027. https://doi.org/10.1017/S1431927611006003.

[11] Liu, C.; Zhang, J.; Ganesh Ramaraj, S.; Zhang, X.; Muruganathan, M.; Mizuta, H.; Oshima, Y. Current Effect on Suspended Graphene Nanoribbon Studied Using in–Situ Transmission Electron Microscopy. *Appl. Surf. Sci.* **2022**, *573*, 151563. https://doi.org/10.1016/j.apsusc.2021.151563.

[12] Choi, W.; Seo, Y.-S.; Park, J.-Y.; Kim, K. B.; Jung, J.; Lee, N.; Seo, Y.; Hong, S. Effect of Annealing in Ar/H_2 Environment on Chemical Vapor Deposition-Grown Graphene Transferred With Poly (Methyl Methacrylate). *IEEE Trans. Nanotechnol.* **2015**, *14* (1), 70–74. https://doi.org/10.1109/TNANO.2014.2365208.

[13] Su, L.; Yu, Y.; Cao, L.; Zhang, Y. In Situ Monitoring of the Thermal-Annealing Effect in a Monolayer of MoS_2. *Phys. Rev. Appl.* **2017**, *7* (3), 034009. https://doi.org/10.1103/PhysRevApplied.7.034009.

Chapter 5 Indirect Electron Beam Gating of MoS_2 Devices

Introduction

This chapter shows the *in-situ* experimental results on electron beam-induced modulation in two-terminal MoS_2 devices. Chapter 5.1 introduces the measurement setup using a sharply focused STEM beam placed near the device, enabling non-contact gating via the SiN_x substrate. Chapter 5.2 discusses the I_{ds}–V_{ds} characteristics under different beam currents. Chapter 5.3 focuses on the time-resolved response of the device, revealing a reversible gating effect with an exponential decay upon beam-off. Chapter 5.4 verifies the electrostatic origin of this effect by excluding thermal contributions and fitting EIS data from SiN_x membranes to an RC circuit model, with results consistent with the observed transient behavior.

5.1 Indirect beam gating measurement of MoS_2 device

As introduced in Chapter 1.3, indirect electron beam gating was recently proposed as a promising method to modulate 2D device electrical conductance. Das and Drndić have proposed an indirect beam gating approach for an *in-situ* TEM two-terminal platform.[1] The advantages of this method include the absence of electron irradiation damage to the target 2D material, electrostatic gating by charge accumulation on the supporting film, and relatively simple device fabrication processes. They showed that irradiating an electron beam onto the SiN_x film near MoS_2 nanoribbons modulated the I_{ds}–V_{ds} characteristics of the MoS_2 channel. In their study, the drain-source current was reduced when the electron beam was irradiated onto the SiN_x film, which was explained by electrostatic charge accumulation in the film due to emission of secondary electrons. However, since the SiN_x film is positively charged, electrons are thought to accumulate near the interface with the film in the MoS_2 layer and act as carriers. It means that electron irradiation may increase the drain-source current, which cannot explain their results. Additionally, the positive charge is expected to be determined by the balance between the number of secondary electrons emitted and the release of charge through the source electrode or silicon substrate connected to ground. It means that the amount of the accumulated positive charge depends on the electron irradiation current.

In this study, we investigated changes in drain-source current (I_{ds}) caused by electron beam irradiation of the insulating film supporting the MoS_2 nanoribbon as well as its dependence on electron beam current (I_{beam}) by our developed *in-situ* TEM measurement. While the concept of an "indirect beam gate" is the same as the previous research, our experimental configuration introduces key differences, including precise control over sample configuration, beam diameter, and beam localization. These differences enable us to clarify the underlying indirect gating mechanism by isolating the contribution of substrate charging to I_{ds} modulation, while preventing direct electron beam exposure to the MoS_2 channel. The mechanism is further supported by impedance spectroscopy, and the proposed model between I_{ds} and I_{beam} is consistent with classical dielectric charging models. Specifically, we demonstrate that the enhancement of I_{ds} is measured when a convergent electron probe irradiates the SiN_x substrate ~15 μm away from a mechanically exfoliated MoS_2 nanoribbon, in contrast to the conductance suppression observed in the previous study when a broad, unfocused TEM beam is applied directly onto CVD-grown MoS_2 flakes.

Figure 5.1(a) shows the schematic image of the experimental system using a custom-designed *in-situ* TEM holder.[2] The nanoribbons of a few layers were placed across a 5 μm gap between two chromium/gold electrodes (source and drain), each 10 μm wide. The

device was built on a 200 μm-thick Si substrate coated with a 50 nm-thick SiN_x film. The SiN_x film at the TEM chip window is suspended to ensure electron transparency. STEM observation was achieved by JEM-ARM 200F at an accelerating voltage of 120 kV. A sharp electron probe was irradiated at a lateral offset of 15 μm from the nanoribbons onto the SiN_x film. The electron beam current I_{beam} was tuned from the lowest illumination current to the highest one by adjusting the illumination settings, which could be measured by a small fluorescent screen located in the viewing chamber, ranging from approximately 840 pA to 35 pA. The diameter of the sharp electron probe was approximately 0.09 nm. The MoS_2-based device was measured using a semiconductor parameter analyzer (Keithley 4200). The I_{ds}–V_{ds} curve of the MoS_2 nanoribbon was systematically measured by changing the I_{beam}.

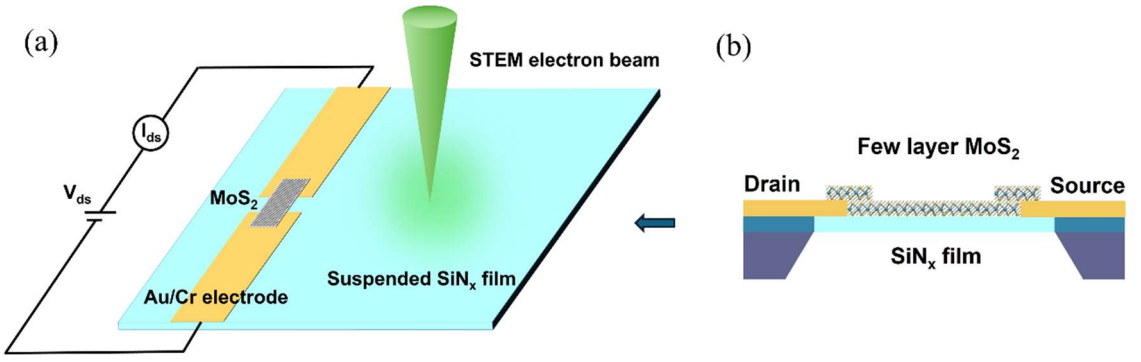

Figure 5.1 (a) Schematic diagram of the MoS_2 device and its cross-section. STEM electron beam (green) exposure at 15μm from the side of a MoS_2 flake. V_{ds} and I_{ds} correspond to drain-source voltage and drain-source current. (b) The cross-section schematic of the MoS_2 device in (a).

The overall chip size was approximately 2.6 × 2.6 mm. Three 60 × 60 μm square windows were etched to form suspended, electron-transparent SiN_x regions. Source and drain electrodes with a width of 10 μm were deposited across the SiN_x windows. The *in-situ* holder sets three tungsten probes serving as source terminal connectors, with a common drain electrode connected via a metal-pressed sheet, as shown in Figure 5.2(a). Three independent devices enable parallel observation.

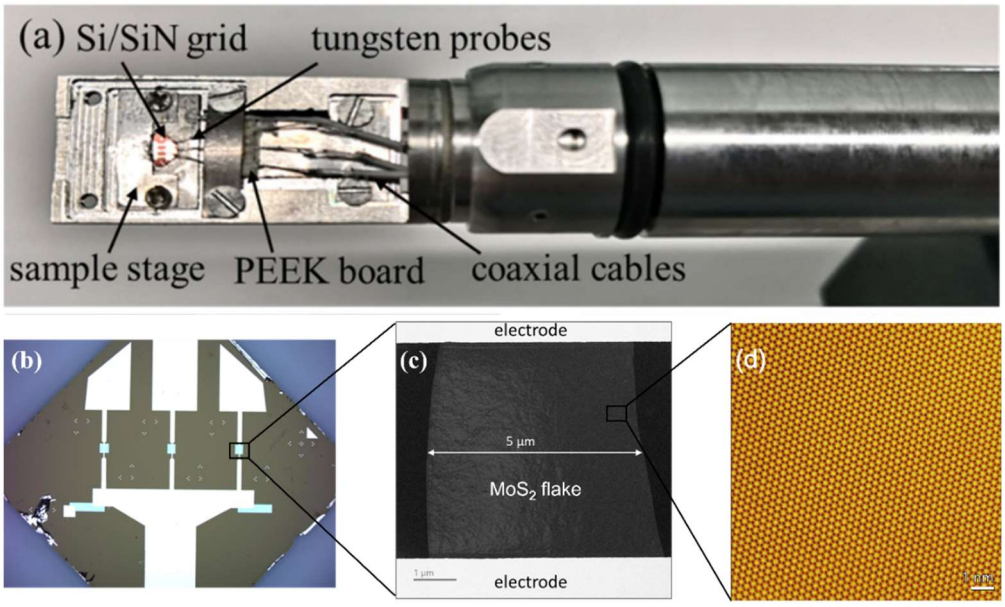

Figure 5.2 (a) Photograph of the sample stage at the head of our developed TEM holder.[2] (b) Optical microscope image of fabricated MoS_2 device based on Si/SiN_x substrate. Three small squares correspond to the windows for TEM observations. (c) The low magnification TEM image of MoS_2 flake cross on the source and drain electron, the flake width is 5μm. The gap between the source and drain is also 5μm. (d) The high magnification BF STEM image of MoS_2 flake.

The MoS_2 flakes were mechanically exfoliated from bulk crystals (HQ Graphene) onto SiO_2/Si substrates. MoS_2 flakes with widths of ~5 μm were pre-selected under an optical microscope, and their thicknesses were then verified via Raman spectroscopy to be approximately 10 layers[3], as shown in Figure 5.3. To protect the fragile SiN_x film and reduce surface contamination during transfer, our improved PPC-based dry transfer method was used to place the MoS_2 flakes between the source and drain electrodes, as shown in Chapter 3.

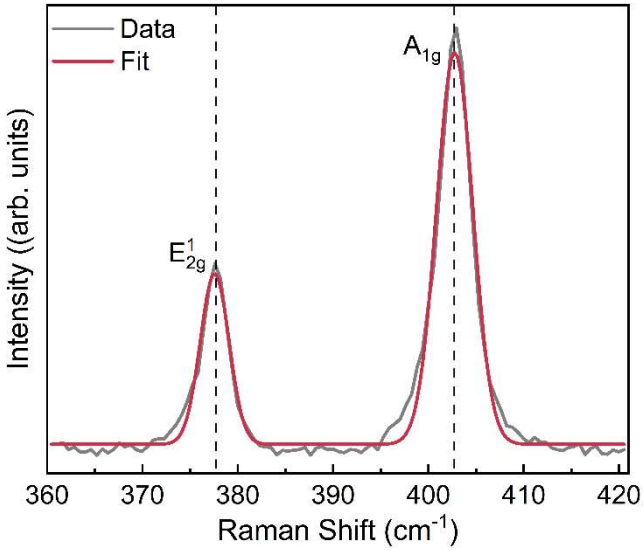

Figure 5.3 Raman characterization of the MoS_2 nanoribbon showing the E^1_{2g} and A_{1g} peaks excited by a 532 nm laser. The peak positions are approximately 378 cm^{-1} and 402 cm^{-1}, respectively, with a frequency difference of approximately 25 cm^{-1}, indicating 10 layers of MoS_2.[3] The red line represents the fitted result.

5.2 *I–V* Characterization and Beam-Induced Modulation Behavior

To clarify the carrier type and normal state of the MoS_2 nanoribbons, it was placed on a metal stage (see illustration inserted in Figure 5.4(a), and the I_{ds} passing through the MoS_2 nanoribbons was measured by sweeping an applied voltage to the metal as a gate voltage, when the drain-source bias voltage (V_{ds}) was fixed to be 0.5 V as shown in Figure 5.4(b). The drain-source current (I_{ds}) was about 135 nA at zero gate voltage, reflecting the n-type conduction behavior of MoS_2. As the gate voltage (V_g) increased from −0.2 V to +0.2 V, the drain current gradually increased, indicating that the accumulation of electrons increases in MoS_2 channels. It can also be explained by the typical behavior of an n-type semiconductor.

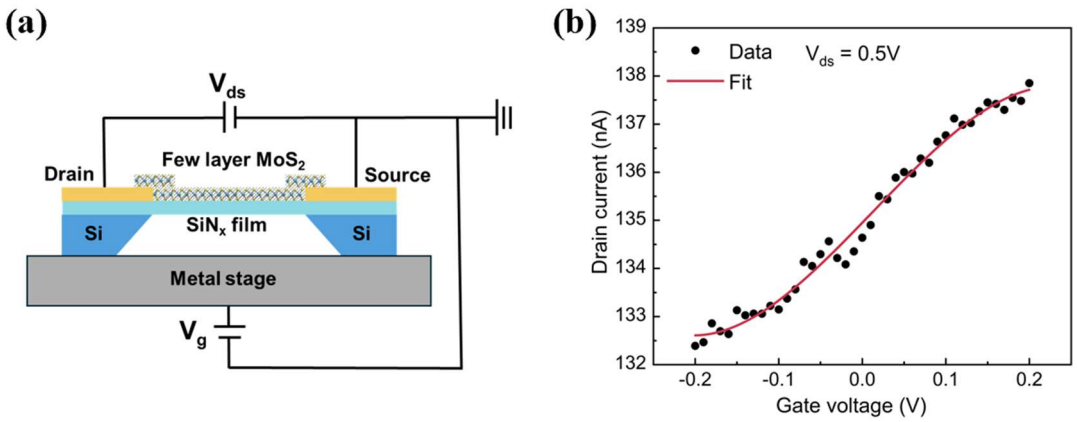

Figure 5.4 (a) The schematic of the measurement setup to clarify the carrier type and normal state. (b) graph of source-drain current as a function of the gate voltage in the rage of ±0.2 V at a constant V_{ds} of 0.5V by setting the device on a metal stage.

Figure 5.5 shows the I_{ds}–V_{ds} curves of the MoS_2 channel when sweeping the V_{ds} from

−2.5 V to +2.5 V under different I_{beam} from 35 pA to 840 pA as mentioned above. The curves are nearly symmetric, indicating the balanced carrier injection at both electrodes. The electron affinity of MoS_2 (about 4.0 eV) is lower than the work function of Au (about 5.4 eV), thus forming a Schottky barrier at the metal-semiconductor interface.[4] Below the bias voltage of ±0.5 V, the I_{ds}–V_{ds} curve shows a linear response, governed by thermionic emission over the Schottky barrier. Above ±0.5 V, it shows a non-linear response, suggesting that the tunneling transport is dominant.[4] Despite the beam being positioned 15 μm away from the MoS_2 channel, a pronounced increase in I_{ds} with increasing I_{beam}. This indicates that the beam irradiation enhances the conductance of the MoS_2 channel via the substrate-mediated mechanism. Obviously, these results suggest that the amount of the positive charges accumulated in the SiN_x film may increase with increasing I_{beam}.

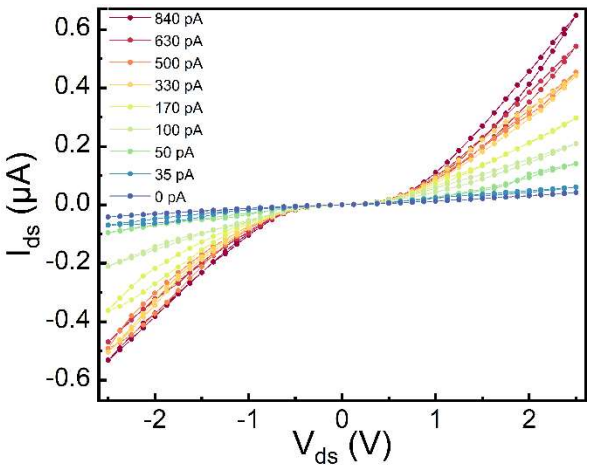

Figure 5.5 Current-voltage (I_{ds}–V_{ds}) curves of the MoS_2 device for each electron beam current from 0 to 840 pA.

The relationship between I_{beam} and I_{ds} is plotted in Figure 5.6 at several drain-source voltages (V_{ds} = 0.5 V, 1.0 V, 1.5 V, 2.0 V, and 2.5 V). At each V_{ds}, I_{ds} rises quickly with increasing I_{beam}, and gradually approaches saturation. Such a relationship between I_{beam} and I_{ds} was fitted for each V_{ds} using an exponential saturation function:

$$I_{ds} = I_{sat}(1 - e^{-\frac{I_{beam}}{I_c}}) \qquad 5-1$$

This model is commonly used to describe input-saturation phenomena, such as activation-limited processes or threshold-based modulation.[5,6] Here, the I_{sat} is the saturation current of the MoS_2 channel under a given V_{ds}, and I_c marks the transition point at which the modulation efficiency starts to decline. The relationship between the measured I_{beam} and I_{ds} is found to be fitted well by Equation 5-1 regardless of V_{ds} as shown in Figure 5.6 (a).

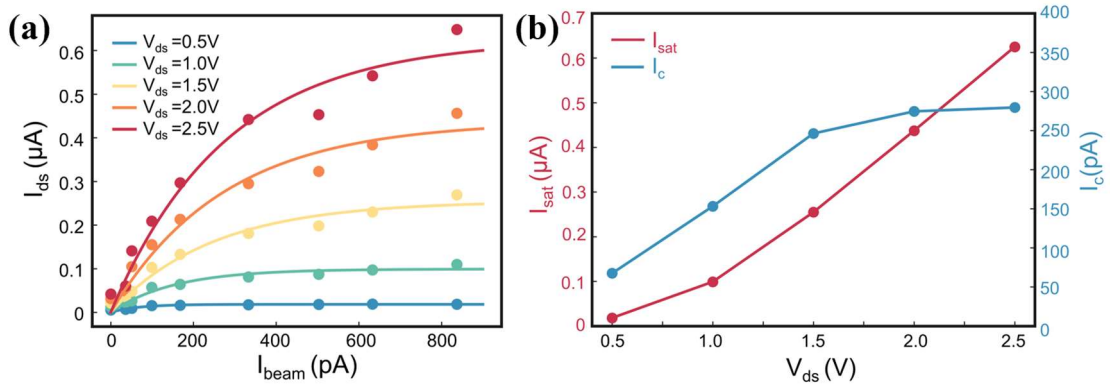

Figure 5.6 (a) Channel current I_{ds} as a function of beam current I_{beam} at various bias voltages (V_{ds} = 0.5–2.5V). (b) Channel saturation current I_{sat} (red) and critical beam current I_c (blue) of the current saturation model in (b) at various bias voltages.

In this study, we suppose that the number of electron carriers in the MoS_2 channel increases in proportion to the amount of positive charge accumulated in the SiN_x film and also that the amount of the positive charge is determined by the balance between the amount of secondary electrons emitted in proportion to the amount of electron beam irradiation and the current flowing to ground through the Si substrate and electrodes. This result suggests that there is an upper limit to the number of secondary electrons emitted when increasing the amount of electron beam irradiation, based on our assumption.

We also notice that I_{ds} is proportional not only to the density of electron carriers but also to the electric field in the MoS_2 channel due to applied V_{ds}. To investigate this point, I_{sat} and I_c values were estimated for each V_{ds} of 0.5 V, 1.0 V, 1.5 V, 2.0 V, and 2.5 V as shown in Figure 5.6 (b). We find that I_{sat} roughly increases in proportion to V_{ds} as 1 V or higher, although it gradually increases below 1 V. In detail, I_{sat} increases by approximately 0.2 μA with each increment of 0.5 V from 1.0 V to 2.5 V. This result suggests that the voltage drop may be low at the interface of the MoS_2 channel and electrodes due to the tunneling transport and that the effective bias voltage applied to the MoS_2 channel may be almost proportional to V_{ds}.

On the other hand, I_c is observed to increase in proportion to V_{ds} from 0.5 to 1.5 V and seems to be constant at 2 V and 2.5 V. Considering Equation 5-1, we expect that I_c does not depend on V_{ds} but on I_{beam} and it must be a constant value against V_{ds}. It may also be caused by the voltage drop at the interface.

5.3 Time-resolved current measurements of MoS_2 device

If the carrier concentration in the MoS_2 channel is related to the number of positive

charges accumulated in the SiN_x film, I_{ds} should change over time depending on whether electron irradiation is turned on or off. Figure 5.8 shows the time evolution of I_{ds} at V_{ds} of 0.01 V and I_{beam} of 100 pA, when turning the electron irradiation on and off. In Figure 5.8 (a), I_{ds} sharply decreases at the same time when turning the electron irradiation off and it slowly decreases after that, following an exponential decrease with a time constant $\tau \approx 90$ s. The sharp decrease can be explained by the immediate cessation of secondary electron emission. While, the slow decrease can be explained by the slow release of accumulated charges, since the SiN_x film has high electrical resistance. Figure 5.8 (b) shows the result of repeatedly turning the electronic irradiation on and off, demonstrating the reproducibility of the decay behavior. When the electron irradiation started to be turned on, I_{ds} sharply increased, and it gradually increased after that. The sharp increase can be explained by the immediate onset of secondary electron emission. The gradual increase may be related to the rising temperature. By fitting an exponential function to the experimental results, the time constant was scattered in the range of 58 to 98 seconds. Such a variation in the time constant is thought to reflect accumulated charge, temperature distribution, and other factors. When highly accelerated electrons are irradiated onto a thin insulator, in addition to atom knock-on and charge up due to secondary electron emission, temperature rise due to phonon excitation also occurs.[7] Due to the low thermal

conductivity of insulators, it must take milliseconds for the temperature to be moderated by heat diffusion.[1] Therefore, the results of Figure 5.8 support our assumption that the amount of the positive charge is determined by the balance between the amount of secondary electrons emitted in proportion to the amount of electron beam irradiation and the current flowing to ground through the Si substrate and electrodes.

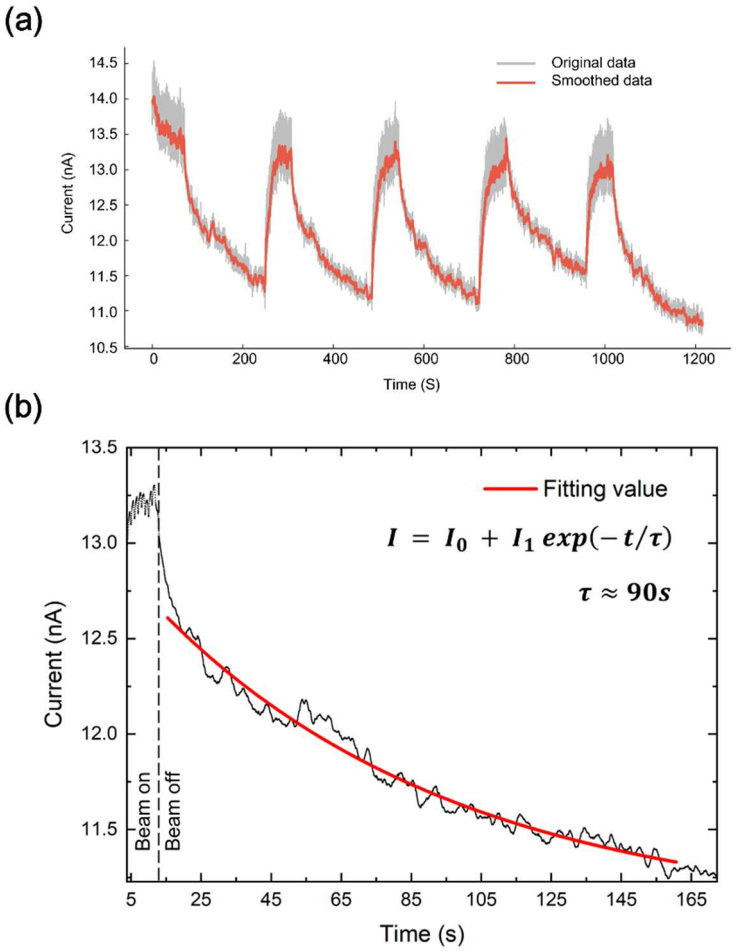

Figure 5.8 (a) Time-resolved response of MoS_2 device to the on-off state of STEM electron beam, on for 10s and off for 180s. (b) The single exponential decay model fits with the off state with a characteristic discharge time of $\tau \sim 90$ s.

To clarify the origin of the indirect beam gating modulation, we performed control measurements on bare SiN_x membranes without MoS_2. No measurable current was detected under varying beam intensities, ruling out direct conduction through the dielectric. However, the *I–V* curves exhibited clear hysteresis, suggesting intrinsic charge trapping and release. This behavior could arise from the ejection of secondary electrons under STEM irradiation, which leads to a local charge imbalance and leaves the SiN_x positively charged. The resulting electrostatic field may act as a local gate, modulating the potential near the MoS_2 channel.

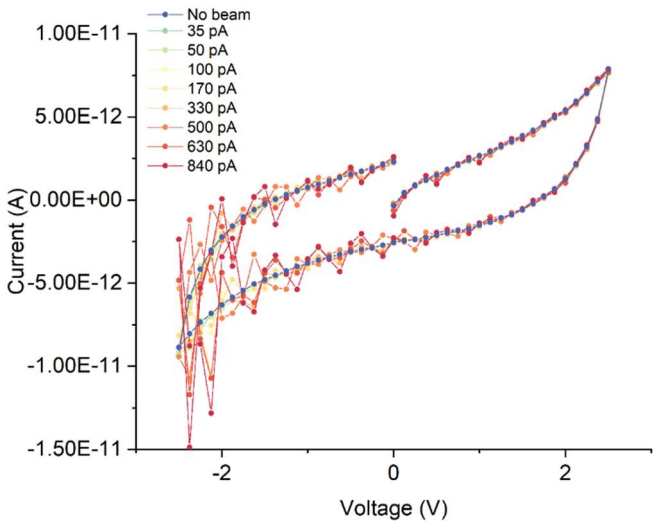

Figure 5.7 *I-V* curve of bare SiN_x with different electron beam strength, showing a clear hysteresis effect. The current of 10^{-12} is much smaller than the 10^{-7} in the *I-V* curve of the MoS_2 device.

5.4 Verification of the Electrostatic Gating Mechanism

Electron irradiation of insulating TEM specimens has been studied previously and results in radiation damage through primarily three modes: knock-on collisions, radiolysis, and electrostatic charging.[8] In the former, atoms in the specimen get displaced via momentum transfer with energetic 120 keV electrons, resulting in defects and vacancies.

In the case of radiolysis, incident electrons cause in-plane vibrational excitations within the specimen, which lead to a localized temperature increase. While a thermoelectric effect has been previously demonstrated in MoS_2 and would explain the correlation here between I_{ds} and I_{beam}, we calculate an estimated heat dissipation time. At 300K, the thermal diffusivity α is noted as[9]:

$$\alpha \approx 9.65 \times 10^{-6} \frac{m^2}{s} \quad 5\text{-}2$$

Then, the characteristic time for heat to diffuse over a distance L is estimated by:

$$\tau \approx \frac{L^2}{\alpha} \quad 5\text{-}3$$

Assuming L is 30 μm, from the center of a 60 × 60 μm SiN_x film, the estimated heat diffusion time is:

$$\tau \approx \frac{(3 \times 10^{-5})^2}{(9.65 \times 10^{-6})} \approx 9.33 \times 10^{-5}\, s \quad 5\text{-}4$$

which is significantly shorter compared with the observed decay in I_{ds} shown in

Figure 5.8 (b). Both knock-on collisions and radiolysis are hence not likely causes of the observed gating effect.

To further verify the charging mechanism, we subsequently conducted electrochemical impedance spectroscopy (EIS) on the same device structure without the MoS_2 channel, as shown in Figure 5.9.

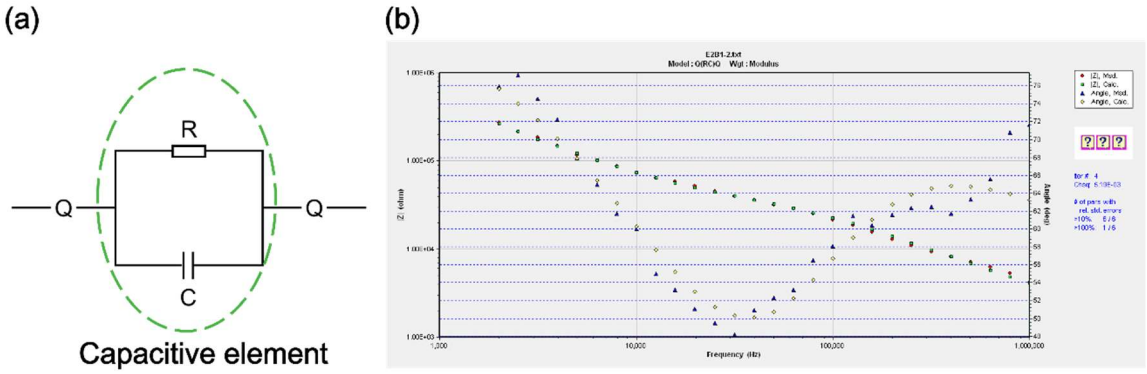

Figure 5.9 (a) Equivalent circuit used to fie the measured bare SiN_x device. (b) EIS Bode plot of the impedance magnitude (|Z|, left y-axis) and phase angle (right y-axis) as a function of frequency for the fitted Q(RC)Q equivalent circuit model.

The measured impedance data are shown as red circles for |Z| and blue triangles for phase angle, while the corresponding fitted values are represented by green squares and yellow diamonds, respectively.

Au electrodes were deposited on a suspended SiN_x membrane, and the resulting Nyquist plot was fitted using an equivalent circuit of the form Q–(R // C)–Q. In this model,

the two Q elements represent constant phase elements (CPEs) that capture the non-ideal interfacial behavior at the Au/SiN_x contacts. These are commonly attributed to effects such as microscopic surface roughness, interfacial states, or spatial inhomogeneities in the potential distribution.

The central (R‖C) unit models the intrinsic electrical behavior of the insulating SiN_x layer. The resistance (R) reflects the leakage resistance of the dielectric, while the capacitance (C) corresponds to the ability of the SiN_x film to store charge at its interfaces or within trap states. From the fitting results in Figure 5.8 (b), we extracted a capacitance of $C = 1.198 \times 10^{-10}\ F$. Then we measured the DC resistance of bare SiN_x film device $R = 3.51 \times 10^{11}\ \Omega$. We calculate the RC time constant τ using the following relation:

$$\tau = R \cdot C \approx 42\ s \tag{5-5}$$

This time constant is in the same order of magnitude as the characteristic decay times (~90 s) observed in the time-resolved current response of MoS_2 under electron beam switching. This supports the accumulation of positive charges in the SiN_x film due to electron irradiation and their release upon turning the irradiation off. Note that in the case of classical RC charging, the charging function is expressed as follows:

$$Q(t) = Q_{max}(1 - e^{-t/RC}) \tag{5-6}$$

where *Q(t)* is the charge stored on the capacitor at time t, and Q_{max} is the maximum charge

corresponding to the applied voltage. This charging accumulation behavior well reproduces the measured time evolution of I_{ds} during turning the electronic irradiation on and off (Fgure5.8). These results supports our assumption that the number of electron carriers in the MoS_2 channel increases in proportion to the amount of positive charge accumulated in the SiN_x film.

Previous studies have also shown that electron beam irradiation in vacuum can induce charge accumulation on suspended dielectric films like SiN_x.[10-12] Specifically, in MoS_2 devices supported on SiN_x films, beam exposure leads to transient current increases during irradiation, and a persistent current decreases after the beam is turned off, with decay times of 80–100 s.[11] These effects are attributed to positive charge accumulation in the insulating film, which behaves analogously to a local gating field.[13] The long relaxation time is consistent with the high resistance of the SiN_x membrane, which slows the discharge of accumulated charges. In our case, although the electron beam does not directly irradiate the MoS_2 channel but rather the adjacent SiN_x film, a clear modulation effect is still observed, supporting the presence of an indirect electrostatic gating effect.

5.5 Discussion of indirect beam gating

Therefore, while irradiated by STEM electron beam, the secondary electron loss in the SiN_x occurred the positive charging of SiN_x film, as is shown in Figure 5.10. It presents a schematic illustration of the energy band structure of the MoS_2 nanodevice before and

after irradiation of a sharp electron probe on SiN_x substrate. In the absence of beam irradiation, the electron affinity of SiN_x is about 2.2 eV.[14] When the MoS_2 contacts with SiN_x, the alignment of the Fermi levels causes the electronic bands of MoS_2 to bend upward. By electron beam irradiation, secondary electron emission from the SiN_x surface leads to net positive charge accumulation in the dielectric. This accumulation induces an effective electrostatic potential (V_{eff}) across the MoS_2/SiN_x interface, which is not externally applied but arises from local charging of the substrate. We suppose that this effective potential ($V_{eff} > 0$) may mimic the effect of a positive gate bias, despite the absence of a physical gate electrode. It creates an internal electric field directed into the MoS_2 channel, resulting in downward band bending and electron accumulation. Therefore, the channel current increases, enabling indirect, non-invasive modulation of MoS_2 devices under *in-situ* TEM conditions.

The current modulation induced by indirect electron irradiation in this study yielded results opposite to the previous report. In the previous report, the current in the MoS_2 channel decreased upon electron irradiation. As mentioned in the introduction, the experimental conditions, such as the electron irradiation region and the arrangement of the MoS_2 layer being measured, differed from those in previous studies. These differences in experimental conditions undoubtedly had an influence on the current in the MoS_2

channel. For example, in the previous study, the dimension of the MoS_2 monolayer film was several times larger than the electrode size and was supported on a SiN_x film. Additionally, since the electron beam was irradiated in the TEM mode, where the electron beam is nearly parallel, some of the electron beam may have directly irradiated the MoS_2 monolayer. In this case, the current in the MoS_2 channel decreases due to secondary electron emission from the MoS_2 monolayer.

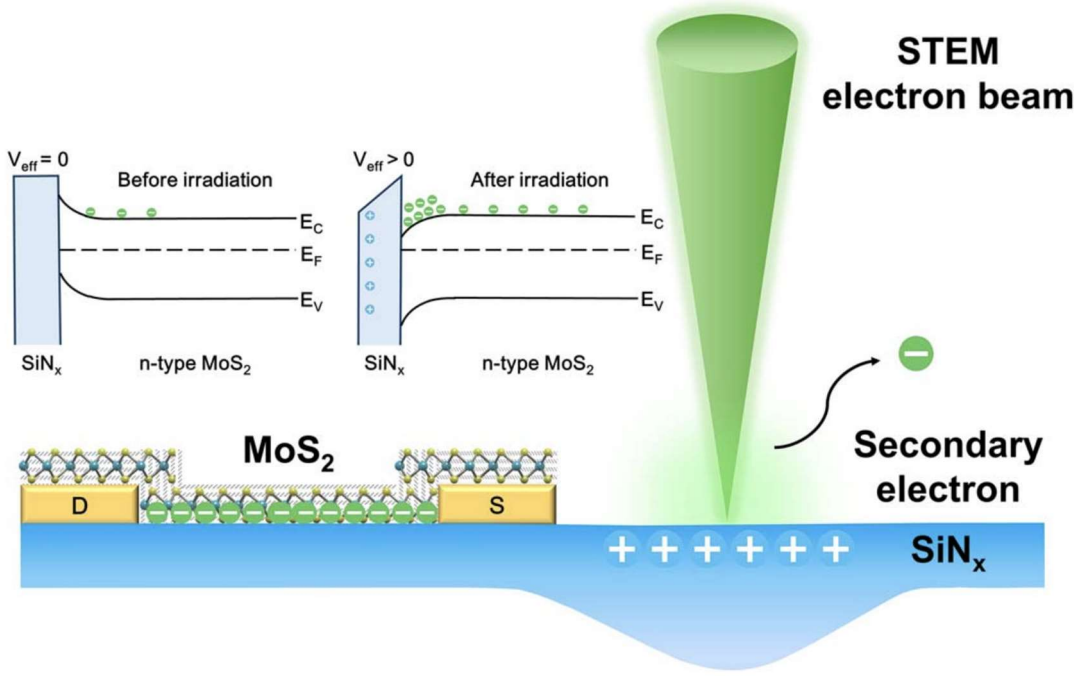

Figure 5.10 Schematic illustration of the energy band structure of MoS_2 nanodevice without and with STEM electron beam irradiation on SiN_x. Beam-induced secondary electron emission leads to positive charge accumulation in SiN_x, creating an effective potential ($V_{eff} > 0$) at the MoS_2/SiN_x interface. This results in downward band bending

and carrier accumulation in MoS_2.

Reference

[1] Masih Das, P.; Drndić, M. In Situ 2D MoS_2 Field-Effect Transistors with an Electron Beam Gate. *ACS Nano* **2020**, *14* (6), 7389–7397. https://doi.org/10.1021/acsnano.0c02908.

[2] Liu, C.; Zhang, J.; Zhang, X.; Muruganathan, M.; Mizuta, H.; Oshima, Y. *In-situ* Electrical Conductance Measurement of Suspended Ultra-Narrow Graphene Nanoribbons Observed via Transmission Electron Microscopy. *Nanotechnology* **2020**, *32* (2), 025710. https://doi.org/10.1088/1361-6528/abbca7.

[3] Li, X.; Han, W.; Wu, J.; Qiao, X.; Zhang, J.; Tan, P. Layer-Number Dependent Optical Properties of 2D Materials and Their Application for Thickness Determination. Adv. Funct. Mater. 2017, 27 (19), 1604468. https://doi.org/10.1002/adfm.201604468.

[4] Das, S.; Chen, H.-Y.; Penumatcha, A. V.; Appenzeller, J. High Performance Multilayer MoS2 Transistors with Scandium Contacts. *Nano Lett*. **2013**, 13 (1), 100–105. https://doi.org/10.1021/nl303583v.

[5] Mitta, S. B.; Choi, M. S.; Nipane, A.; Ali, F.; Kim, C.; Teherani, J. T.; Hone, J.; Yoo, W. J. Electrical Characterization of 2D Materials-Based Field-Effect Transistors. *2D Mater*. **2021,** 8 (1), 012002. https://doi.org/10.1088/2053-1583/abc187.

[6] Syu, T.; Abdel-Motaleb, I. M. An Analytical AlGaAs MODFET Charge Control

Model for Computer Aided Design Applications. *In Proceedings of the 32nd Midwest Symposium on Circuits and Systems*,; **1989**; pp 1263–1266 vol.2. https://doi.org/10.1109/MWSCAS.1989.102086.

[7] Feng, G.-B.; Wang, F.; Hu, T.-C.; Cao, M. Characteristics of Charge and Discharge of PMMA Samples Due to Electron Irradiation. Chin. Phys. B 2015, 24 (11), 117901. https://doi.org/10.1088/1674-1056/24/11/117901.

[8] Egerton, R. F.; Li, P.; Malac, M. Radiation Damage in the TEM and SEM. Micron 2004, 35 (6), 399–409. https://doi.org/10.1016/j.micron.2004.02.003.

[9] Incropera, F.; DeWitt, D.; Bergman, T.; Lavine, A. Fundamentals of Heat and Mass Transfer; 2007.

[10] Li, H.; Liu, C.; Zhang, Y.; Qi, C.; Wei, Y.; Zhou, J.; Wang, T.; Ma, G.; Tsai, H.-S.; Dong, S.; Huo, M. Electron Radiation Effects on the Structural and Electrical Properties of MoS2 Field Effect Transistors. Nanotechnology 2019, 30 (48), 485201. https://doi.org/10.1088/1361-6528/ab3ce2.

[11] Yu, B.; Sun, M.; Pan, R.; Tian, J.; Zheng, F.; Huang, D.; Lyu, F.; Zhang, Z.; Li, J.; Chen, Q.; Li, Z. Semi-Custom Methodology to Fabricate Transmission Electron Microscopy Chip for in Situ Characterization of Nanodevices and Nanomaterials. Sci. China Technol. Sci. 2022, 65 (4), 817–825. https://doi.org/10.1007/s11431-021-

1980-1.

[12] Guo, H.; Maus-Friedrichs, W.; Kempter, V.; Shi, J. A Study of the Charging Phenomena during Electron Irradiation of Sintered Si3N4. Nucl. Instrum. Methods Phys. Res. Sect. B Beam Interact. Mater. At. 2001, 173 (4), 463–469. https://doi.org/10.1016/S0168-583X(00)00431-6.

[13] Mkrtchyan, M.; Gasparyan, A.; Mkhoyan, K.; Liddle, A.; Novembre, A.; Muller, D. SCALPEL Mask-Membrane Charging. Microelectron. Eng. 1999, 46 (1), 223–226. https://doi.org/10.1016/S0167-9317(99)00067-2.

[14] Gritsenko, V. A.; Dikovskaja, N. D.; Mogilnikov, K. P. Band Diagram and Conductivity of Silicon Oxynitride Films. Thin Solid Films 1978, 51 (3), 353–357. https://doi.org/10.1016/0040-6090(78)90299-7

Chapter 6

Summary

In this thesis, indirect electron beam gating of in two-terminal MoS_2 devices has been investigated using in-situ STEM techniques. Such indirect beam irradiation led to a pronounced, reversible modulation of the channel conductance.

Chapter 1 introduces TMDCs family and its benchmark member MoS_2. MoS_2 offers unique electrical properties desirable for nanoscale electronics. Conventional modulation strategies, including doping and back-gating, face limitations in spatial resolution and compatibility with in-situ measurements. In-situ TEM provides an alternative platform capable of correlating atomic structure with electronic behavior in real time. We further introduce indirect electron beam gating as an emerging modulation approach and position it as the focus of this study.

In Chapter 2, we detail the experimental methodology for conducting *in-situ* TEM studies on MoS_2 transistors. The devices were fabricated on suspended SiN_x membranes patterned with Cr/Au electrodes. A custom-designed TEM chip, together with a home-built *in-situ* holder, enabled simultaneous electron beam irradiation and electrical biasing. This integrated setup establishes a stable platform for investigating beam-induced modulation in MoS_2 devices.

Chapter 3 describes the development of an optimized dry-transfer process. By replacing conventional PDMS with a PPC/PDMS composite stamp, we achieved precise pick-up and controlled release of MoS_2 flakes. The improved thermal control of PPC minimized contamination and mechanical strain on the SiN_x substrate. Optical microscopy and STEM imaging confirm successful and clean transfer. The dry transfer process enables reproducible fabrication of beam-compatible devices and is crucial for achieving stable electrical measurements in the TEM environment.

Chapter 4 highlights the critical importance of contamination control in *in-situ* TEM studies, where beam-induced deposition or surface residues can significantly affect measurement accuracy. To address this, we introduce a series of surface cleaning strategies for 2D material devices. In particular, Ar/H_2 atmosphere annealing was employed both before and after the transfer of MoS_2 flakes—first to pre-clean the TEM chip, and then to remove residual polymers following transfer. STEM imaging confirms the successful removal of contaminants and the restoration of atomically clean MoS_2 surfaces.

Chapter 5 systematically investigates the indirect electron beam gating effect in two-terminal MoS_2 devices using a sharply focused STEM probe. When the beam irradiates the SiN_x substrate that 15 μm away from the MoS_2 channel, a clear and reversible increase

in channel current is observed, despite the absence of direct exposure. The I_{ds}–V_{ds} curves exhibit nonlinear behavior typical of Schottky-type transport, with the current increasing significantly under higher beam intensities. Time-resolved measurements show that the beam-induced conductance decays exponentially after switching off the beam, with a characteristic time constant $\tau \approx 90$ s. Impedance spectroscopy performed on bare SiN_x membranes revealed an RC time constant of approximately 42 s, consistent with the charging–discharging behavior seen in MoS_2 devices. These findings support a model where the STEM beam induces electrostatic charging of the dielectric substrate, which in turn modulates the carrier injection at the MoS_2 interface. The results demonstrate the feasibility of using indirect electron beam gating as a non-contact modulation strategy and provide new insights into charge-dielectric interactions in 2D electronic systems.

Acknowledgements

First and foremost, I would like to express my deepest gratitude to my supervisor, Prof. Yoshifumi Oshima, for his unwavering support, insightful guidance, and continuous encouragement throughout my doctoral studies. His patience and optimism inspired me to persevere, especially when facing challenges in my experiments. With his mentorship, I was able to complete this work and enjoy a fulfilling academic journey at JAIST.

I am also sincerely grateful to Assoc. Prof. Chunmeng Liu in Zhengzhou University for her generous support. From the beginning, she provided hands-on training in experimental operations and continuously offered invaluable suggestions regarding research design, data analysis, and manuscript writing.

My appreciation further extends to Prof. Yukiko Yamada-Takamura, Prof. Hiroshi Mizuta, and their group members for providing access to experimental facilities and offering thoughtful advice. I am particularly grateful to Dr. Afsal from the Mizuta Lab, who demonstrated the dry transfer technique for substrate devices in detail. His instruction laid the foundation for my development of the PPC-based dry transfer method used in this study.

I would like to thank Prof. Kosuke Nagashio and Asst. Prof. Kanahashi for their kind support and valuable discussions on semiconductor device physics. After the visit to

Nagashio lab, I greatly broadened my understanding of device fabrication and characterization.

Special thanks are also due to Lecturer Aso and senior lab members in Oshima Lab—Assoc. Prof. Zhang, Dr. Xie, Dr. Chiew, Dr. Chen—for their helpful discussions and experimental advice. I am grateful to my lab mates, Mr. Xu, Mr. Xiong, Mr. X. Liu, Ms. Yang and Ms. Nakashima, for their collegiality and stimulating conversations.

I would like to acknowledge the financial support from the China Scholarship Council, which made this research possible. Finally, I extend my heartfelt thanks to my parents, my friend Ms. Shi, Dr Song and Ms Zhang, and Mr. Li, for their unconditional love and encouragement throughout this journey. I am deeply thankful to everyone who has supported me, both academically and personally, in completing this dissertation.

List of publications

[1] Chen, L.; Liu, C.; Oshima, Y. In-situ TEM Observation of Electron Irradiation Gate Effect in MoS_2 Nanoribbon Channels. Jpn. J. Appl. Phys. 2025, 64 (8), 085001.

[2] Matsuyama, K.; Chen, L.; Aso, K.; Kanahashi, K.; Nagashio, K.; Oshima, Y.; Kiriya, D. Phase Engineering of 1T′-MoS_2 via Organic Enwrapment. J. Am. Chem. Soc. 2025, 147 (20), 16729–16734. https://doi.org/10.1021/jacs.5c02099.

[3] Yang, X.; Zhang, Y.; Chen, L.; Aso, K.; Yamamori, W.; Moriya, R.; Watanabe, K.; Taniguchi, T.; Sasagawa, T.; Nakatsuji, N.; Koshino, M.; Yamada-Takamura, Y.; Oshima, Y.; Machida, T. Intrinsic One-Dimensional Moiré Superlattice in Large-Angle Twisted Bilayer WTe_2. ACS Nano 2025, 19 (13), 13007–13015. https://doi.org/10.1021/acsnano.4c17317.

[4] Kanahashi, K.; Tanaka, I.; Nishimura, T.; Aso, K.; Lu, A. K. A.; Morito, S.; Chen, L.; Kakeya, T.; Watanabe, S.; Oshima, Y.; Yamada-Takamura, Y.; Ueno, K.; Azizi, A.; Nagashio, K. Dimensionality-Induced Transition from Degenerate to Nondegenerate States in Nb-Doped WSe_2. ACS Nano 2025, 19 (10), 10244–10254. https://doi.org/10.1021/acsnano.4c17660.

List of conferences

International Conference (Oral Presentation)

[1] Chen, L.; Liu, C.; Liu, F.; Afsal, K.; Muruganathan, M.; Mizuta, H.; Oshima, Y. Electrical Conductance of Suspended MoS_2 Nanoribbon Measured by In-situ Transmission Electron Microscope. The 4th East-Asia Microscopy Conference (EAMC4), 1–4 December 2022, Taipei.

International Conference (Poster Presentation)

[1] Chen, L.; Liu, C.; Liu, F.; Afsal, K.; Mizuta, H.; Oshima, Y. Fabrication of MoS_2 Nanoribbon by Direct Transfer for In-situ TEM Observation. National Conference on Electron Microscopy, 17–21 October 2024, Dongguang.

[2] Chen, L.; Liu, C.; Liu, F.; Afsal, K.; Muruganathan, M.; Mizuta, H.; Oshima, Y. Electrical Conductance of Suspended MoS_2 Nanoribbon Measured by In-situ Transmission Electron Microscope. The 20th International Microscopy Congress (IMC-20), 10–15 September 2023, Busan.

[3] Chen, L.; Liu, C.; Liu, F.; Afsal, K.; Muruganathan, M.; Mizuta, H.; Oshima, Y. Fabrication of MoS_2 Nanoribbon by Direct Transfer for In-situ TEM Observation. The 22nd International Vacuum Congress (IVC-22), 11–16 September 2022, Sapporo.

Domestic Conference (Poster Presentation)

[1] Chen, L.; Liu, C.; Liu, F.; Afsal, K.; Mizuta, H.; Oshima, Y. Electrical Conductance of Suspended MoS_2 Nanoribbon Measured by In-situ Transmission Electron Microscope. The 67th Fullerenes-Nanotubes-Graphene General Symposium, 1–3 September 2024, Kochi.

[2] Chen, L.; Liu, C.; Liu, F.; Afsal, K.; Mizuta, H.; Oshima, Y. Electrical Conductance of Suspended MoS_2 Nanoribbon Measured by In-situ Transmission Electron Microscope. JAIST International Symposium of Nano-Materials for Novel Devices, 11–12 January 2024, Kanazawa.